

GyPSuM: A joint tomographic model of mantle density and seismic wave speeds

Nathan A. Simmons,¹ Alessandro M. Forte,² Lapo Boschi,³ and Stephen P. Grand⁴

Received 9 April 2010; revised 30 July 2010; accepted 17 August 2010; published 1 December 2010.

[1] GyPSuM is a 3-D model of mantle shear wave (S) speeds, compressional wave (P) speeds, and density. The model is developed through simultaneous inversion of seismic body wave travel times (P and S) and geodynamic observations while using realistic mineral physics parameters linking wave speeds and density. Geodynamic observations include the global free air gravity field, divergence of the tectonic plates, dynamic topography of the free surface, and the flow-induced excess ellipticity of the core-mantle boundary. GyPSuM is built with the philosophy that heterogeneity that most closely resembles thermal variations is the simplest possible solution. Models of the density field from Earth's free oscillations have provided great insight into the density configuration of the mantle but are limited to very long wavelength solutions. Alternatively, scaling higher-resolution seismic images to obtain density anomalies generates density fields that do not satisfy geodynamic observations. The current study provides a 3-D density model for the mantle that directly satisfies geodynamic and seismic observations through a joint seismic-geodynamic inversion process. Notable density field observations include high-density piles at the base of superplume structures, supporting the general results of past normal mode studies. However, we find that these features are more localized and have lower amplitude than past studies would suggest. When we consider both fast and slow seismic anomalies in GyPSuM, we find that P and S wave speeds are strongly correlated throughout the mantle. However, we find a low correlation of fast S wave zones in the deep mantle (>1500 km depth) with the corresponding P wave anomalies, suggesting a systematic divergence from simplified thermal effects in ancient subducted slab anomalies. The cratonic lithosphere and D'' regions are shown to have strong compositional signatures. However, we argue that temperature variations are the primary cause of P wave speed, S wave speed, and density anomalies throughout most of the mantle.

Citation: Simmons, N. A., A. M. Forte, L. Boschi, and S. P. Grand (2010), GyPSuM: A joint tomographic model of mantle density and seismic wave speeds, *J. Geophys. Res.*, **115**, B12310, doi:10.1029/2010JB007631.

1. Introduction

[2] Evaluating the relative behavior of various mantle properties is a powerful way to identify compositional variations and processes occurring in the mantle [e.g., Robertson and Woodhouse, 1996; Su and Dziewonski, 1997; Kennett et al., 1998; van der Hilst and Kárasoñ, 1999; Ishii and Tromp, 1999, 2004; Masters et al., 2000; Saltzer et al., 2001; Kennett and Gorbatov, 2004; Trampert et al., 2004; Khan et al., 2009]. It has been well established that correlation of shear and bulk sound speeds reduce in the deep mantle

(lowest ~1000 km) and are likely anticorrelated in some regions [e.g., Su and Dziewonski, 1997; Kennett et al., 1998; Masters et al., 2000]. Moreover, studies incorporating normal mode splitting functions have provided evidence that high-density piles exist at the base of the mantle where “superplumes” may originate, thereby contradicting the simple assumption that deep mantle heterogeneities are produced solely by temperature variations [e.g., Ishii and Tromp, 1999; Trampert et al., 2004]. On the basis of very long wavelength images of the mantle, it has been argued that chemical variations dominate thermal heterogeneity and therefore buoyancy forces in the deep mantle [Trampert et al., 2004]. However, density and wave speed heterogeneities derived from normal mode splitting data that are only sensitive to the longest length scale heterogeneities provide a limited understanding of the structure and dynamics of Earth's mantle. These data appear to be subject to considerable trade-offs and nonuniqueness [Kuo and Romanowicz, 2002], and moreover, the inferred density anomalies provide poor fits to fundamental long-wavelength surface geodynamic constraints [Soldati et al., 2009].

¹Atmospheric, Earth and Energy Division, Lawrence Livermore National Laboratory, Livermore, California, USA.

²GEOTOP, Département des Sciences de la Terre et de l'Atmosphère, Université du Québec à Montréal, Montreal, Quebec, Canada.

³Eidgenössische Technische Hochschule Hönggerberg, Institute of Geophysics, Zurich, Switzerland.

⁴Jackson School of Geosciences, University of Texas at Austin, Austin, Texas, USA.

Table 1. Constraints on Mantle Heterogeneity Employed in This Study

Constraint	Description	Quantity	Source
S waves	Residual travel times for globally distributed S , ScS , sS , $sScS$, SKS , $SKKS$ phases. Data also include surface reflected multiples (e.g., SSS , $ScS3$, etc.) and triplicated phases turning within the upper mantle.	~46,000	Grand [2002] Simmons et al. [2007]
P waves	Residual travel times for teleseismic P waves based on a recompilation of International Seismic Centre (ISC) data (EHB). Arrivals are condensed using a summary ray approach over $2^\circ \times 2^\circ$ bins.	~626,000	Engdahl et al. [1998] (EHB) Antolik et al. [2003]
Gravity	Global free air gravity field from the EGM96 geopotential model derived from a compilation of land-, air-, and space-based observations.	spherical harmonic degrees 2–16	Lemoine et al. [1998]
Plate motions	Divergence of all tectonic plates calculated from the NUVEL-1 plate velocity model.	spherical harmonic degrees 1–16	DeMets et al. [1990]
Dynamic topography	Nonisostatic topography of Earth's free surface. Estimated from removal of the crustal isostatic topography signal on the basis of CRUST2.0.	spherical harmonic degrees 1–16	Bassin et al. [2000] Forte and Perry [2000]
CMB ellipticity	Excess ellipticity of the core–mantle boundary (CMB) relative to Earth's surface. The CMB is elevated by ~400 m along the equator according to studies of Earth's free core nutation processes.	zonal harmonic degree 2	Herring et al. [2002] Mathews et al. [2002]
Mineral physics parameters	Bounds on the relative heterogeneity ratios ($R_{\rho/S} = d \ln \rho/d \ln V_S$ and $R_{P/S} = d \ln V_P/d \ln V_S$) due to pure thermal variations. Anharmonic and anelastic effects included.	N/A	Karato and Karki [2001] Cammarano et al. [2003]

[3] In order to better understand the dynamics of the mantle, we must first know the density anomalies that drive mantle flow. One way to estimate density anomalies in the mantle is through the translation of a pure seismically derived velocity model to density anomalies through application of mineral physics relationships. Most often, the density models resulting from this approach provide less than satisfactory fits to key geodynamic observations such as the global free air gravity anomalies derived from satellite data [Forte, 2007]. Thus, this approach requires the introduction of strong compositional effects to fit geodynamic data leading to potential overestimates of nonthermal contributions to mantle heterogeneity [Simmons et al., 2009]. Although geodynamic observations are sensitive to global integrals of 3-D anomalies throughout the mantle, these observations alone cannot adequately resolve local density structure within the mantle. Therefore, seismic observations are required to define the local 3-D distribution of seismic heterogeneity, which can then be interpreted in terms of density anomalies. In our previous studies [Simmons et al., 2006, 2007, 2009], we combined geodynamic observations and S wave travel times in global scale simultaneous inversions for S wave speed and density. In these studies, both types of data were directly inverted to produce the 3-D models of density and seismic velocity as opposed to estimating density anomalies through a posteriori scaling of a pure seismically derived model.

[4] The benefit of joint inversion of multiple types of data is multifold. First, joint inversion directly accounts for the variable resolution of individual data sets that might produce quite different distributions of mantle heterogeneities when considered alone. In addition, simultaneous inversion of different forms of information allows for the determination of multiple mantle properties that are most consistent with one another given some underlying hypothesis such as the dominance of

thermal effects. Moreover, we can more accurately evaluate the relative behavior of mantle properties as determined through a direct joint inversion process, since the model parameterization and roughness levels are equivalent. In other words, the joint inversion process removes a number of biases that would potentially lead to unnecessarily large degrees of compositional influence to explain multiple observations simultaneously.

[5] In this paper, we present the GyPSuM model (G = geodynamic, P = compressional waves, S = shear waves, M = mineral physics), which represents the next step in the evolution of a detailed multicomponent mantle model presented in our previous studies [Simmons et al., 2006, 2007, 2009]. As in our previous studies, GyPSuM is constructed through the simultaneous inversion of seismic and geodynamic constraints using mineral physics relationships that relate to the mantle properties. Also similar to our previous model developments, we simultaneously consider globally distributed S wave arrival times, the global free air gravity field, divergence of the tectonic plates, dynamic topography of Earth's free surface, and the flow-driven excess ellipticity of the core–mantle boundary (CMB). The most important improvement from our previous studies is the incorporation of globally distributed P wave travel time measurements, thus allowing the generation of a detailed, three-component mantle model (density, P wave velocity, and S wave velocity). We also perform nonlinear inversions to gradually adjust heterogeneities and mineral physics relationships rather than the pure linear approach employed in the previous studies.

2. Seismic and Geodynamic Data

[6] The seismic data used in this study consist of globally distributed, teleseismic S wave and P wave travel time observations (Table 1) that are not restricted to common source–

receiver pairs. The S wave observations consist of ~46,000 travel time residuals derived from waveforms band-pass filtered from 0.01 to 0.07 Hz. The seismic phases include S , ScS , sS , $sScS$, SKS , and $SKKS$ phases including surface-reflected multiples (e.g., SSS) and triplicated phases turning within the upper mantle [Grand, 1994, 2002; Grand *et al.*, 1997; Simmons *et al.*, 2006, 2007, 2009]. Travel time residuals are relative to a 1-D model consisting of an average of the TNA/SNA models in the upper mantle [Grand and Helmberger, 1984] and PREM in the lower mantle [Dziewonski and Anderson, 1981]. Corrections for crustal structure and ellipticity are based on the CRUST5.1 model of Mooney *et al.* [1998] and the techniques developed by Dziewonski and Gilbert [1976], respectively. Earthquake locations were determined through an iterative process, which involved tomographic inversions followed by event relocation in several steps [Simmons *et al.*, 2006]. We view these data as highly reliable, given that they are based on meticulous analyses of synthetic waveform correlation and detailed event modeling. Also, given the diverse suite of phases reflecting and refracting through the mantle and our selection of evaluated earthquakes, the coverage of the mantle is maximized. For more information regarding these data (measurement procedures, coverage, etc.), see Grand [1994, 2002] and Simmons *et al.* [2006, 2007].

[7] The P wave observations consist of ~626,000 summary travel time residuals computed in Antolik *et al.* [2003]. The underlying data come from the recompilation and relocation of the International Seismological Centre (ISC) direct P wave arrivals performed by Engdahl *et al.* [1998] (EHB). The seismic events were relocated on the basis of the S&P12/WM13 3-D model [Su and Dziewonski, 1993] and subsequently summarized on a $2^\circ \times 2^\circ$ global grid and 50–100 km event depth increments [Antolik *et al.*, 2003]. The original ISC arrivals are not based on the more reliable waveform correlation techniques employed in the generation of the S wave data set; however, the level of scrutiny involved in the grooming of the P wave data by Engdahl *et al.* [1998], the summary data analysis of Antolik *et al.* [2003], and the large amount of data yields a valuable set of global P wave observations. Similar to the corrections applied to the S wave data, these data were corrected on the basis of CRUST5.1 as well as the ellipticity of Earth.

[8] The set of geodynamic constraints we employ consists of a suite of convection-related observables sensitive to the viscosity of the mantle, the style of mantle flow, and 3-D density variations. These surface observables include the free air gravity field from the EGM96 geopotential model derived through a compilation of land-, air-, and space-based observations [Lemoine *et al.*, 1998]. These gravity data provide robust constraints on density anomalies in both the upper and lower mantles, with maximum sensitivity shifting to the upper mantle as the horizontal wavelength decreases.

[9] In addition, we employ constraints derived from the observed tectonic plate motions as given by the NUVEL-1 plate velocity model in the no-net-rotation (NNR) frame of reference [DeMets *et al.*, 1990, 1994; Argus and Gordon, 1991]. For a given plate geometry, assuming the plates are rigid bodies, it can be shown that a scalar representation of the plate velocity field in terms of its horizontal divergence (along ridges and trenches) provides a sufficient description of the surface kinematics [Forte and Peltier, 1994]. The radial

vorticity of the plate motions (along transform boundaries) is a linear function of the horizontal divergence, and it does not provide additional independent information on plate kinematics in the NNR reference frame [Forte and Peltier, 1994]. We therefore employ the horizontal divergence field derived from the NUVEL-1 (NNR) velocities as a constraint on buoyancy forces in the mantle. According to the mantle flow theory (outlined in section 3), the tectonic plate motions are coupled to the underlying mantle flow driven by density anomalies, and they are thus important constraints on 3-D density heterogeneity in the midmantle (at longest wavelengths) and the upper mantle (at shorter wavelengths).

[10] We also consider the dynamic topography of Earth's free surface estimated by the removal of the crustal isostatic topography signal [Forte and Perry, 2000]. These data are the least robust in the suite of geodynamic observations given the uncertainties of the global crustal structure; however, crust-corrected dynamic surface topography is a direct mapping of vertical stresses in the mantle and thus provides important constraints on the range of upper mantle density configurations needed to explain the other geodynamic observations considered.

[11] Large-scale mantle flow driven by density anomalies has a direct impact on the overall shape of the CMB [see Forte *et al.*, 1995] and may account for the ~400 m of excess bulge along the equator [Herring *et al.*, 2002; Mathews *et al.*, 2002]. Therefore, we also incorporate the excess ellipticity of the CMB observed from Earth's free core nutation processes as an additional constraint on mantle density [Herring *et al.*, 2002; Mathews *et al.*, 2002]. The full suite of data related to mantle convection employed as the geodynamic constraints in the joint inversions is shown in Figure 1. The harmonic coefficients used to synthesize the fields in Figure 1 are the elements of the data vector, \mathbf{g} , in the forward system of equations outlined in section 3. See Table 1 for a summary of all of the seismic and geodynamic constraints employed in this study.

3. Forward Model

[12] The forward model consists of a combined set of seismic and geodynamic observations that are linearly related to seismic velocity and density anomalies in a set of blocks representing the mantle. The blocks are approximately 275×275 km in lateral dimension at all depths. Depth ranges are variable with 22 layers from 75 to 240 km thick, providing a total of 99,148 model parameters. The seismic sensitivities were computed through 1-D ray tracing (infinite frequency approximation) to form a set of sensitivity (Fréchet) kernels for both the S and P data sets individually. The individual sets of kernels provide the basis for the linear equations relating travel times and S wave slowness perturbations, which are internally translated to P wave slowness perturbations through scaling relationships discussed below.

[13] Geodynamic sensitivity kernels were computed from the theoretical linear relationship between mantle density anomalies and each of the surface observables (free air gravity field, plate divergence, dynamic surface topography, and excess CMB ellipticity). This requires an analytical description of the viscous flow response of the mantle to internal point sources of density for each convection-related observation [Richards and Hager, 1984; Ricard *et al.*, 1984; Forte

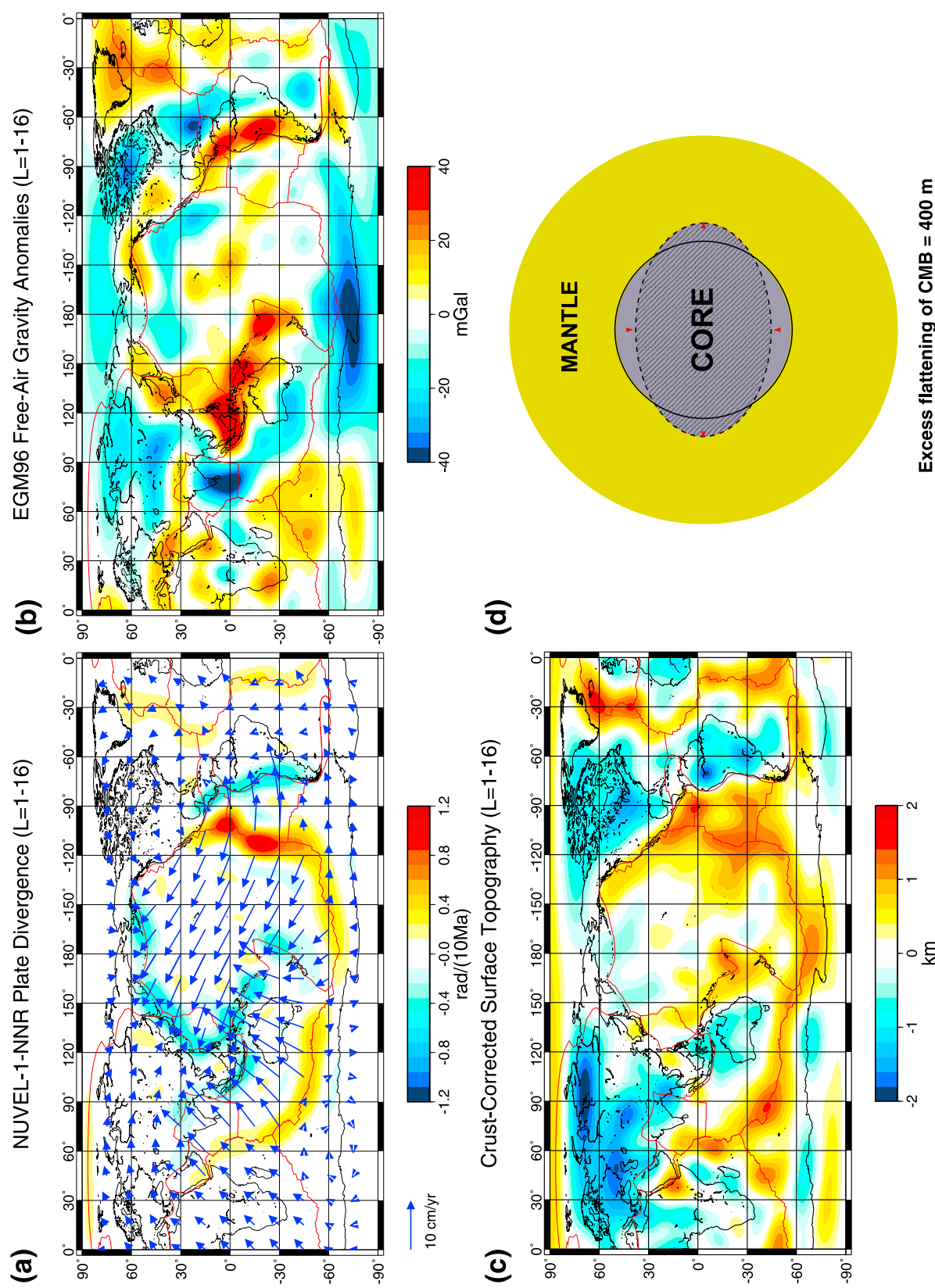


Figure 1

and Peltier, 1987]. We computed viscous flow responses for a compressible and gravitationally consistent mantle whereby tectonic plate motions are dynamically coupled to the underlying mantle flow [Forte and Peltier, 1994; Forte, 2007]. A combination of mixed free-slip and no-slip surface boundary conditions were incorporated to calculate the responses assuming the radially symmetric viscosity profile derived from joint inversion of convection data and glacial isostatic adjustment (GIA) observations [Mitrovica and Forte, 2004]. On the basis of the study of Simmons et al. [2006], the viscous flow responses were determined with the assumption that a whole-mantle style of flow prevails. Therefore, no strict boundaries to vertical mass transport are incorporated into building the responses with the exception of the CMB and the free surface. Each of the geodynamic data fields has a unique sensitivity to the mantle that varies with the harmonic degree or corresponding horizontal wavelength (Figure 2). Thus, simultaneously considering the entire suite of geodynamic observations provides significant constraints on the 3-D arrangement of density anomalies that may exist in the mantle.

[14] The mantle flow theory employed in making the connection (via the geodynamic kernels) between lateral heterogeneity in the mantle and the convection data does not explicitly model the effects arising from lateral viscosity variations (LVV) in the mantle. It is worth noting, however, that the geodynamically inferred radial viscosity profile we employ [Mitrovica and Forte, 2004] in calculating the kernels has embedded in it the depth-dependent horizontal average of the LVV [Moussa et al., 2007]. In this case, provided we use this mean viscosity profile, the effect of LVV on the predicted convection-related observables is of the same order (or smaller) than the current uncertainties in the global tomography models [Moussa et al., 2007]. Furthermore, as shown by Wen and Anderson [1997], LVV at shallow depths have the largest impact on the predicted surface motions, particularly in terms of generating realistic amplitude surface divergence and radial vorticity. The tectonic plates themselves arguably constitute the largest-amplitude manifestation of LVV anywhere in the mantle, and the plate-coupled mantle flow theory we employ [Forte, 2007] explicitly models the impact of rigid surface plates on the underlying mantle flow.

[15] Expressing the seismic and geodynamic observations as a single set of linear equations yields a large and complex system best described in the following matrix form,

$$\begin{bmatrix} \mathbf{L}_S \\ \lambda_P \mathbf{L}_P(R_{P/S}, V_S/V_P) \\ \lambda_G \mathbf{G}(R_{\rho/S}, -V_S) \\ \lambda_{CMB} \mathbf{c}(R_{\rho/S}, -V_S) \\ \lambda_D \mathbf{D} \end{bmatrix} \Delta \mathbf{m}_S = \begin{bmatrix} \mathbf{r}_S \\ \lambda_P \mathbf{r}_P \\ \lambda_G \mathbf{g} \\ \lambda_{CMB} \mathbf{e} \\ \mathbf{0} \end{bmatrix}, \quad (1)$$

where \mathbf{L}_S and \mathbf{L}_P are the S and P wave sensitivity kernel matrices and \mathbf{r}_S and \mathbf{r}_P are the corresponding travel time residuals. The gravity, dynamic topography, and plate divergence sensitivities and harmonic coefficients (data) are represented by \mathbf{G} and \mathbf{g} , respectively. Similarly, the excess CMB ellipticity sensitivity and degree 2 harmonic coefficient are represented by \mathbf{c} and \mathbf{e} . The matrix \mathbf{D} represents a second-order digital smoothing filter with 76% of the weight applied to the lateral elements (blocks) and 24% of the weight applied to the vertical elements (depth extent). For the purpose of clarity, all terms in equation (1) are summarized in Table 2.

[16] In equation (1), the goal is to solve for an S wave slowness perturbation model, $\Delta \mathbf{m}_S$. Therefore, the P wave sensitivities (\mathbf{L}_P) and geodynamic sensitivities (\mathbf{G} and \mathbf{c}) are associated to S wave slowness perturbations through relative heterogeneity ratios ($R_{P/S}$ and $R_{\rho/S}$). Since the relative heterogeneity ratios are represented in terms of seismic velocity perturbations, conversions relating velocity perturbations (ΔV) to slowness perturbations (Δs) were also propagated through the sensitivity kernel matrices using the approximation $\Delta V/V_0 \approx -V_0 \Delta s$ (where V_0 is the background velocity).

[17] One of the major issues when attempting to simultaneously invert multiple forms of data is determining the relative weights for each set of observations (λ_P , λ_G , and λ_{CMB} in equation (1)). It might seem reasonable to dramatically down-weight the P wave data set relative to the S wave data set given the ~14-fold increase in the number of P wave data. However, simply defining λ_P on the basis of number of observations is not ideal since P wave travel time residuals are systematically smaller than the S wave residuals. Weighting based on the number of data is particularly problematic when considering S wave phases that travel through the high-amplitude anomalies in the upper mantle multiple times (e.g., SSS) producing very large residual travel times (signals). Therefore, we chose the seismic data set weighting on the basis of the relative data norms,

$$\lambda_P \equiv \frac{\|\mathbf{r}_S\|}{\|\mathbf{r}_P\|}. \quad (2)$$

Equation (2) yields $\lambda_P \approx 0.7$, which provides a suitable data set weight based on our sensitivity tests. The weighting of the geodynamic observations is more difficult, since these data are represented as spherical harmonic coefficients in contrast to travel time residuals. On the basis of our previous joint investigations [Simmons et al., 2006, 2007, 2009], the optimum weighting of the geodynamic observations relative to the S wave data (λ_G) was found to be ~1000. In the current study, we chose to double the weight ($\lambda_G = 2000$) to account for the addition of the P wave observations providing an approximately equivalent influence of geodynamic and seismic observations. λ_{CMB} was chosen to be sufficiently

Figure 1. Geodynamic observables employed in the joint seismic-geodynamic tomography inversions. (a) Blue arrows represent the plate velocity vectors obtained from the NUVEL-1 model [DeMets et al., 1990] relative to a global frame of reference in which there is no net rotation (NNR) of the lithosphere. The color contours represent the rate of horizontal divergence of the plate velocity field. (b) The free air gravity anomalies derived from the joint geopotential model EGM96 [Lemoine et al., 1998]. (c) The dynamic surface topography obtained by removing the topography due to isostatically compensated crustal heterogeneity from Earth's observed topography. The CRUST2.0 [Bassin et al., 2000] crustal heterogeneity model is employed here. (d) The excess or dynamic CMB ellipticity inferred from core nutation data [Mathews et al., 2002]. All fields, with the exception of Figure 1d, have been expanded in spherical harmonics up to degree and order 16.

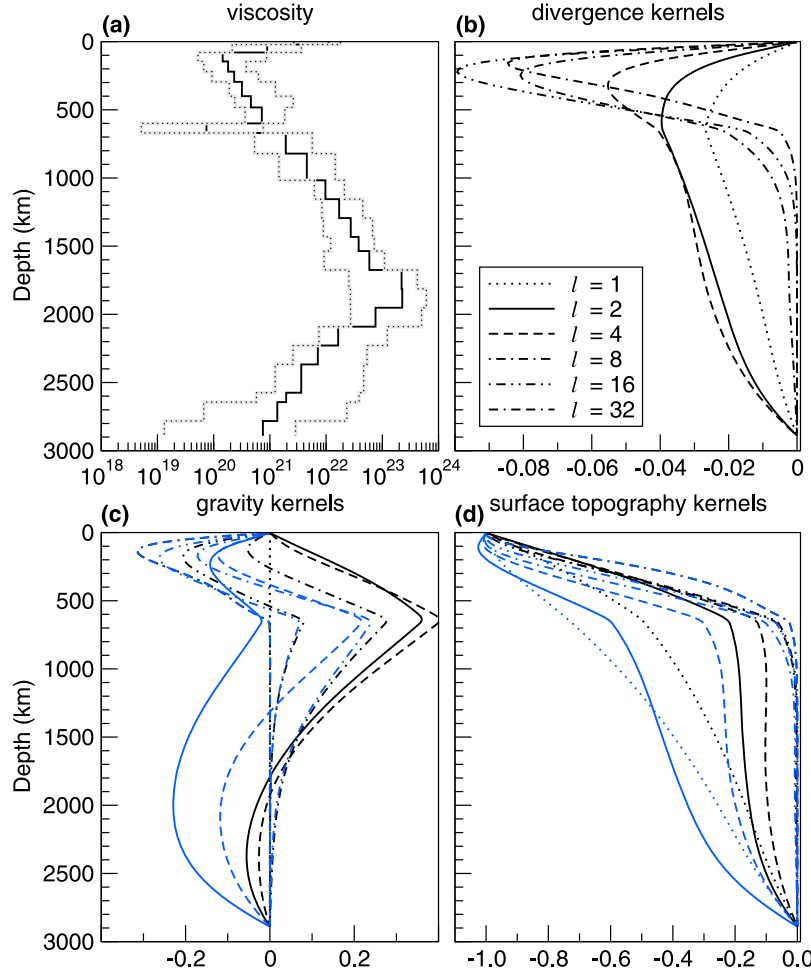


Figure 2. Mantle viscosity and viscous response (kernel) functions. (a) The solid black line depicts the depth variation of effective mantle viscosity derived from the simultaneous Occam-style inversion of mantle convection and glacial isostatic adjustment data sets [Mitrovica and Forte, 2004]. Absolute values of viscosity (in units of 10^{21} Pa s) are plotted. The black-dotted gray lines depict the range of uncertainties in the viscosity inferences derived from the Occam inversion. (b) The wavelength-dependent kernels for the rate of horizontal divergence of the tectonic plates. The inset legend identifies the (reciprocal) wavelengths in terms of equivalent spherical harmonic degrees. (c) The kernels for the free air surface gravity anomalies are represented for free-slip (black curves) and no-slip (blue curves) surface boundary conditions. (d) The dynamic (surface) topography kernels are depicted for free-slip (black curves) and no-slip (blue curves) surface boundary conditions.

large to fully match the observed CMB excess ellipticity similar to the treatment of Simmons *et al.* [2009]. The following sections describe our multistep approach to solving the complicated system described in equation (1).

4. Density- P - S Coupling in a Thermal Scenario

[18] Adopting the philosophy of the joint seismic-geodynamic modeling approach by Simmons *et al.* [2009], we chose to initially attribute mantle heterogeneities to temperature variations and subsequently relax this requirement. This approach involves first determining the optimum scaling relationships ($R_{\rho/S}$ and $R_{P/S}$) that account for the relative behavior of mantle properties when temperature variations are the dominant cause. One of the major issues is the large range of uncertainty of these parameters even when only considering the effects of temperature [see Cammarano

et al., 2003; Karato and Karki, 2001]. To aid in the search for the optimum scaling relationships, it is useful to evaluate how these ratios are related. Using the notation from Karato and Karki [2001], the relative behavior of V_S to density and sound speed can be written,

$$\begin{aligned} R_{\rho/S} &= \frac{2}{(\Gamma - 1) + 2Q_S^{-1}X(\xi)C} \\ R_{\phi/S} &= \frac{\delta_S - 1}{(\Gamma - 1) + 2Q_S^{-1}X(\xi)C} = \frac{\delta_S - 1}{2}R_{\rho/S}, \end{aligned} \quad (3)$$

where ρ , S , and ϕ correspond to density, S wave speed, and sound wave speed respectively. The parameters Γ and δ_S are the Anderson-Grüneisen parameters [e.g., Anderson, 1989] relating differential changes of the elastic moduli to density variations and thus represent the pure elastic effects to the

Table 2. Forward Model Variables

Variable	Description	Details
\mathbf{L}_S	Shear wave sensitivity kernels	1-D raypath lengths $46,000 \times 99,148$ sparse elements
\mathbf{L}_P	Compressional wave sensitivity kernels	1-D raypath lengths $626,000 \times 99,148$ sparse elements
\mathbf{G}	Geodynamic data viscous flow response kernels	Spatial sensitivities of spherical harmonic components up to degree 16; free air gravity, plate divergences, dynamic topography $861 \times 99,148$ full elements
\mathbf{c}	CMB ellipticity kernel	Spatial sensitivity of the degree 2 zonal harmonic $1 \times 99,148$ full elements (row vector)
\mathbf{D}	Regularization operator	Second-order digital smoothing filter
$\lambda_P, \lambda_G, \lambda_{CMB}, \lambda_D$	Weights	Relative weighting between data sets ($\lambda_P, \lambda_G, \lambda_{CMB}$); regularization weight (λ_D)
V_S, V_P, ρ	Wave speeds and density	Starting model velocities and density from PREM and TNA/SNA models (see text)
$R_{\rho/S}$	Compressional/shear wave relative heterogeneity ratio	$R_{\rho/S} = d \ln V_P / d \ln V_S$
$R_{\rho/S}$	Density/shear wave relative heterogeneity ratio	$R_{\rho/S} = d \ln \rho / d \ln V_S$
\mathbf{r}_S	Shear wave travel time residual measurements	$\sim 46,000$ residuals (column vector)
\mathbf{r}_P	Compressional wave travel time residual measurements	$\sim 626,000$ residuals (column vector)
\mathbf{g}	Geodynamic data	Spherical harmonic coefficients up to degree 16 of the free air gravity, plate divergences, dynamic topography; 861 elements (column vector)
e	CMB ellipticity	Degree 2 zonal harmonic coefficient representing 400 m of excess ellipticity on the core-mantle boundary
$\Delta \mathbf{m}_S$	Shear wave slowness perturbation model	Heterogeneity model to be determined through inversion

ratios in equation (3). Q_S is the S wave attenuation parameter, and $X(\xi)C$ is a correction factor for anelasticity. The correction factor $X(\xi)C$ is a product of the frequency dependence of attenuation, activation enthalpy, melting temperature, and the estimated range of lateral temperature variations (see *Karato and Karki* [2001] for a thorough description). Therefore, $2Q_S^{-1}X(\xi)C$ represents the anelastic component to the relative heterogeneity ratios. If we also consider the relationship between the three types of seismic wave speeds, we can readily derive a relationship between $R_{\rho/S}$ and $R_{P/S}$,

$$\frac{\delta V_P}{V_P} = \gamma \frac{\delta V_S}{V_S} + (1 - \gamma) \frac{\delta V_\phi}{V_\phi}, \quad \gamma = \frac{4 V_S^2}{3 V_P^2}$$

$$\Rightarrow R_{P/S} = \frac{(\delta_S - 1)}{2} R_{\rho/S} (1 - \gamma) + \gamma. \quad (4)$$

Note that this simple formulation is identical to *Karato and Karki* [2001] with the assumption that bulk attenuation is negligible, yielding $Q_S/Q_P = \gamma$. Equation (4) shows that for simple thermal variations in the mantle, $R_{\rho/S}$ scales to $R_{P/S}$ in a predictable way. Therefore, equation (4) represents the full $\rho - V_S - V_P$ coupling for thermally induced variations of isochemical mantle material. If we assume that δ_S is a fixed value at any given depth and velocity variations are relatively small, we need only to determine one ratio ($R_{\rho/S}$ or $R_{P/S}$) and directly compute the other, thereby simplifying the optimization problem.

[19] *Simmons et al.* [2009] determined that a simple 1-D representation of $R_{\rho/S}$ was not adequate to account for the relative behavior of density and S wave velocity variations in the mantle. This conclusion was based on the inability to simultaneously explain geodynamic and seismic S wave data with radially symmetric scaling profiles. There are multiple reasons for this, including the existence of compositionally distinct cratonic keels and the dependence of Q_S on the

background temperature. In order to account for these first-order effects, *Simmons et al.* [2009] introduced scaling model correction derivatives of the form,

$$\kappa = \frac{\partial R_{\rho/S}}{\partial \ln V_S}. \quad (5)$$

The search for the optimum κ values yielded highly negative values in the cratonic roots and slightly positive numbers in the noncratonic (“thermal”) upper mantle. Therefore, $R_{\rho/S}$ values in fast cratonic zones were systematically reduced, yielding less negative and sometimes positive buoyancies in accord with the iron depletion hypothesized in these mantle regions [e.g., *Jordan*, 1978]. Similarly, $R_{\rho/S}$ values in the low-velocity, noncratonic upper mantle were significantly reduced in agreement with the expected behavior due to the temperature dependence of Q_S .

5. Modeling Procedures

[20] In our joint modeling approach, we initially performed inversions with simple scaling relationships, thereby forcing the spatial patterns of the heterogeneity fields (density and wave speeds) to be correlated, which is likely an oversimplification [e.g., *Masters et al.*, 2000]. We subsequently allow the spatial patterns of wave speeds and density to deviate from one another in a systematic manner. These deviations in spatial patterns are formed by allowing the scaling relationships ($R_{\rho/S}$ and $R_{P/S}$) to evolve from constant values in a depth layer (1-D) to fully 3-D relationships.

[21] Before proceeding to the joint inversion, we tested the ability of seismic models (derived entirely from seismic data alone) to match the other observations considered in this study. We selected the optimum $R_{\rho/S}^{1-D}$ profile (Figure 3) as well as the TX2008s S wave velocity model from *Simmons et al.* [2009] for evaluation. We note that, although a jointly derived solution (TX2008j) was produced by *Simmons et al.* [2009], we chose to use the pure seismically derived version

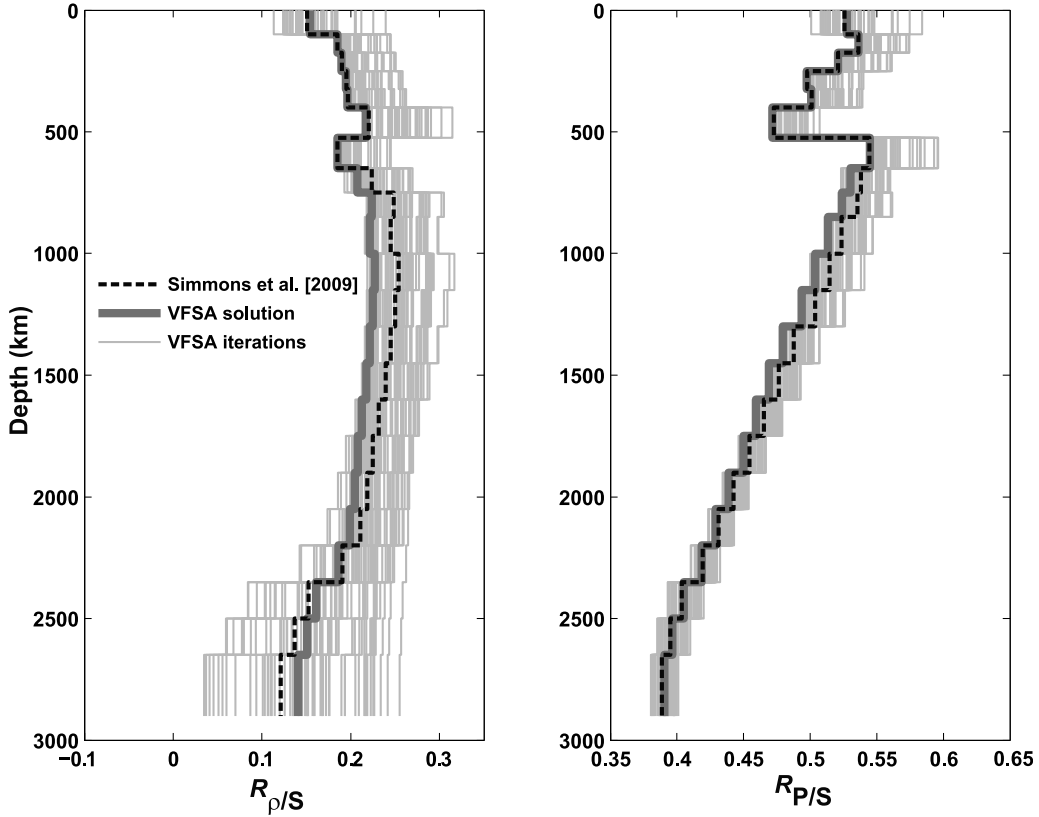


Figure 3. Optimized relative heterogeneity ratios determined through a very fast simulated annealing (VFSA) process. Only the 1-D part of the 1.5-D scaling models are shown. (left) Density-shear scaling relationships including the starting solution from *Simmons et al. [2009]* (dashed line) and the solution found in the current study (thick solid line). Scaling model profiles that were accepted within the VFSA process are also shown (thin gray lines). The allowable range of 1-D solutions was bounded according to the results of *Cammarano et al. [2003]* and *Karato and Karki [2001]*. (right) Optimized 1-D compressional-shear velocity scaling profile based on the fully coupled density-shear-compressional fields and joint inversions (see text). The starting solution and VFSA iterations are similarly shown.

to demonstrate the potential difficulties arising from the use of S wave data alone. For these tests, equation (4) was used to calculate $R_{\rho/S}^{1\text{-D}}$, assuming simple depth-dependent δ_S and γ . In the upper mantle, bulk δ_S values were estimated by comparing the $R_{\rho/S}^{1\text{-D}}$ profile from *Simmons et al. [2009]* and the corresponding $R_{\rho/S}^{1\text{-D}}$ profile computed by *Cammarano et al. [2003]* yielding δ_S values between 2.2 and 3.8. In the lower mantle, we estimated δ_S to be linearly decreasing from 2.7 (top of the lower mantle) to 1.3 (base of the mantle) based on the values for MgSiO_3 perovskite presented by *Karato and Karki [2001]*.

[22] Applying the 1-D scaling profiles to the TX2008s S wave velocity model, we calculated the variance reduction fit to all of the considered data fields (Table 3). The scaled TX2008s model is incapable of satisfying the geodynamic constraints since it is derived solely with S wave constraints as pointed out by *Simmons et al. [2009]*. This scaled S wave model also provides a poor fit to the P wave constraints employed in the current study ($\sim 12\%$ variance reduction). To gain perspective on this measure of P wave data fit, we performed tomographic inversions considering only the P wave data while using the same parameterization and inversion techniques used to develop TX2008s. The inversions were carried out using the iterative LSQR algorithm [*Paige and*

Saunders, 1982] with a spectrum of smoothing weights. The optimum P wave model (henceforth referred to as “P-only”) provided $\sim 32\%$ variance reduction fit to the P wave data set. This relatively low degree of potential fit (compared to the S wave data set and model) is, in part, a product of the signal-to-noise ratio of the residual P wave travel times and is comparable to studies using the same data [e.g., *Antolik et al., 2003*]. The P-only model, when scaled to shear velocities and densities (with $R_{\rho/S}^{1\text{-D}}$ and $R_{P/S}^{1\text{-D}}$), provides a poor level of fit to the S wave data ($\sim 56\%$) and remarkably low degrees of fit to the geodynamic observations as well (Table 3). Clearly, we could likely find a better set of 1-D conversion factors to scale these independently produced models through a trial-and-error process. However, as demonstrated by *Simmons et al. [2009]*, selecting the best fitting scaling model on the basis of a heterogeneity model derived from a single type of data does not necessarily lead to better fitting models after a joint inversion is performed. These tests mainly serve to provide some insight into the potential fit that may be achieved with our model parameterization, and they also provide reference levels for subsequent comparisons.

[23] The initial step in the three-component model construction is the joint inversion for density and wave speed variations while assuming simple 1-D scaling models ($R_{\rho/S}^{1\text{-D}}$

Table 3. Model Fits to All Data Considered^a

Model Name	Scaling Models $R_{\rho/S}$, $R_{P/S}$	S Wave Arrivals (%)	P Wave Arrivals (%)	Free Air Gravity (%)	Tectonic Plate Divergence (%)	Dynamic Surface Topography (%)	CMB Excess Ellipticity (km)
TX2008s ^b	1-D ^c	94	12	1	48	-44	1.3
P-only ^d	1-D ^c	56	32	-57	30	-164	1.3
TX2008j ^b	3-D ^c	93	12	91	99	80	0.4
GyPSuM_1D ^e	1-D ^c	90	28	69	97	-70	0.4
GyPSuM_1.5D ^e	1.5D ^e	90	29	73	97	32	0.4
GyPSuM ^f	3-D ^f	93	31	88	99	72	0.4

^aFits are expressed as variance reduction (in percent) except for excess CMB ellipticity expressed in km (0.4 km is the expected value).

^bShear wave models produced with seismic data alone (TX2008s) and joint inversion of shear wave travel times and geodynamic information (TX2008j) from *Simmons et al. [2009]*.

^cOptimum 1-D and 3-D density-shear scaling models found on the basis of joint seismic-geodynamic inversion [*Simmons et al., 2009*] and computed compressional-shear scaling (see text).

^dCompressional velocity model produced using only P wave data described in the text. TX2008s and P-only have similar model roughness. Models are for fit comparison only.

^eJoint P-S-geodynamic models developed using 1-D scaling (GyPSuM_1D) and a modified scaling model that accounts for first-order effects of cratonic mass depletion and the temperature dependence of Q (GyPSuM_1.5D). Scaling model (1.5-D) was found through the simulated annealing process described in the text.

^fFinal P-S-density and scaling models developed in this study.

and $R_{P/S}^{1-D}$) previously described. The primary reasons for initially solving the system in equation (1) assuming 1-D scaling profiles are to (1) develop an unbiased starting model for scaling model optimization and (2) establish the appropriate level of model roughness when considering the combined data set. The joint solution with 1-D scaling models (“GyPSuM_1D”) provides a more balanced level of fit to the seismic data sets than the independently produced models (variance reduction fit of 90% to the S wave data and 28% to P wave data set). In addition, the fits to the geodynamic observations are dramatically improved with the exception of the dynamic topography, which is still poorly matched (Table 3). The problem of reconciling the dynamic topography and gravity fields simultaneously has been recognized for quite some time [e.g., *Forte et al., 1993; Le Stunff and Ricard, 1995*]. In the context of joint seismic-geodynamic inversion, this problem persists when assuming simple 1-D scaling profiles that force the geographic pattern of wave speed and density perturbations to be identical. However, when directly considering the impact of iron depletion of the cratons and the temperature dependence of Q_S through implementation of scaling model corrections (i.e., equation (5)), the level of fit to the dynamic topography field can be greatly improved while maintaining a good fit to the observed gravity field [*Simmons et al., 2009*]. The search for these scaling model correction terms as well as other free parameters is described in the following section.

5.1. Scaling Model Optimization (1.5-D R Values)

[24] One major limitation of the *Simmons et al. [2009]* investigation was that the determination of the velocity-based correction derivatives (κ terms defined in equation (5)) were based on a fixed (i.e., given) velocity model. In general terms, this is a nonlinear problem since the determination of S wave velocity structure in a joint modeling process is a function of the corrected $R_{\rho/S}$ values and vice versa. In the current study, we wish to find the optimum 1-D scaling models ($R_{\rho/S}$) and correction derivatives (e.g., equation (5)) while considering the nonlinearity of the problem. Since we are also incorporating P wave constraints, the selection of $R_{\rho/S}$ impacts the calculated values of $R_{P/S}$ (via equation (4)) and our ability to simultaneously fit the P wave data set as well.

[25] Given these complexities, we have formulated the scaling model optimization problem by defining a parametric form of $R_{\rho/S}$ in the following way,

$$R_{\rho/S} = aR_{\rho/S}^{1-D} + b + \kappa\delta \ln V_S, \quad (6)$$

where $R_{\rho/S}^{1-D}$ is a starting 1-D scaling model and κ is a velocity-based scaling correction derivative defined in equation (5). The coefficients a and b represent the amplification and baseline shift of the starting 1-D scaling model, respectively. Therefore, a controls the overall shape of the 1-D portion of scaling factor profile, b controls the mean value, and κ adjusts the scaling factor model according to the underlying S wave velocity structure. We will further refer to the dimension of such a scaling model as 1.5-D.

[26] Equation (6) presents the basic form of the optimization problem; however, the coefficients are regionally dependent. Specifically, we define two sets of coefficients ($[a_{um}, b_{um}]$ and $[a_{lm}, b_{lm}]$) that adjust the upper (subscript “um”) and lower mantle (subscript “lm”) scaling models independently. Additionally, we define multiple κ terms to account for the cratonic versus the noncratonic upper mantle zones as well as potential depth dependence of these values. In total, we consider nine free parameters described in Table 4.

[27] To appropriately test the validity of a single set of these nine free parameters, we performed a nonlinear joint inversion involving the iterative updating of scaling models and global heterogeneity models. A grid search or Monte Carlo approach would be computationally daunting, and we have therefore adapted a very fast simulated annealing (VFSA) approach [*Ingber, 1989; Jackson et al., 2004*] to identify the optimum set of scaling model adjustment parameters described in equation (6) and Table 4. Our adaptation of the VFSA process includes a rapid VFSA cooling schedule to limit the number of full joint inversions required (Figure 4). We also limited the range of possible 1-D components of the scaling factors according to the ranges presented in the mineral physics works of *Cammarano et al. [2003]* and *Karato and Karki [2001]*. Additionally, within each VFSA iteration and parameter update, joint inversions of the combined data sets were performed by solving equation (1) using the LSQR

Table 4. Scaling Model Optimization Parameters

General Form: $R_{\rho/S} = aR_{\rho/S}^{1-D} + b + \kappa\delta \ln V_S$		
Parameter	Description	VFSA Solution
$R_{\rho/S}^{1-D}$	Starting density-shear velocity relative heterogeneity ratio from <i>Simmons et al.</i> [2009]	N/A
$\delta \ln V_S$	Shear wave velocity heterogeneity	N/A
κ	Velocity-based scaling model correction derivatives of the form $\partial R_{\rho/S}/\partial \ln V_S$	N/A
a_{um}	Amplification factor applied to the starting 1-D upper mantle density-velocity scaling profile	0.916
b_{um}	Additive term that adjusts the mean of the 1-D upper mantle scaling profile	0.0157
a_{lm}	Amplification factor applied to the starting 1-D lower mantle density-velocity scaling profile	0.651
b_{lm}	Additive term that adjusts the mean of the 1-D lower mantle scaling profile	0.0619
κ_{craton}^{100}	Scaling model correction derivative defined only in the cratonic roots in the upper 100 km	-5.92
κ_{craton}^{250}	Scaling model correction derivative defined only in the cratonic roots from 100 to 250 km depth	-3.13
$\kappa_{thermal}^{100}$	Scaling model correction derivative in the noncratonic upper 100 km	1.26
$\kappa_{thermal}^{250}$	Scaling model correction derivative in the noncratonic mantle in the 100–250 km depth range	1.59
$\kappa_{thermal}^{650}$	Scaling model correction derivative in the noncratonic mantle in the 250–650 km depth range	0.341

algorithm. Thus, joint inversion was embedded within the VFSA process producing a new mantle model with each step to determine if the set of parameters improved the level of fit to all of seismic and geodynamic data.

[28] The VFSA process was terminated after 61 model updates due to the small changes of model parameter and misfit variations at this stage (Figure 4). The 1-D component of the resulting $R_{\rho/S}^{1.5-D}$ relationship (Figure 3) in the upper mantle converged to the lowest allowable values in the upper mantle similar to the results of *Simmons et al.* [2009]. This bias toward the lowest acceptable values in the upper mantle (based on the range for the 1300°C adiabatic calculations by *Cammarano et al.* [2003]) is most likely a product of the combined effects of cratons and high-temperature zones that both require lowered scaling values to account for the iron depletion and the temperature dependence of Q_S , respectively. The strongest upper mantle velocity signatures are “atypical” in that they either deviate from a simple pyrolytic composition or have very high temperature, yet they occupy a large portion of the shallow upper mantle and therefore greatly influence the 1-D scaling model solution.

[29] In the lower mantle, however, we find that the 1-D component differs from the results of *Simmons et al.* [2009], who strictly tested a limited number of possible scaling profiles. In the current case, the 1-D component of the lower mantle $R_{\rho/S}^{1.5-D}$ relationship has lower amplitude in the middle of the mantle and higher amplitude near the base. This “straightening” of the scaling model possibly reflects the

lessening of the contributions of anelasticity relative to the starting model taken from *Karato and Karki* [2001]. The profiles in the work of *Karato and Karki* [2001] might in fact exaggerate the bulk contributions of anelasticity to mantle heterogeneity as recently reported in some mineral physics studies [e.g., *Brodholt et al.*, 2007; *Matas and Bukowinski*, 2007]; our results suggest a similar conclusion. Since the $R_{P/S}$ relationship is tied to the $R_{\rho/S}^{1.5-D}$ relationship for thermally induced variations according to equation (4), the 1-D component of the $R_{\rho/S}^{1.5-D}$ relationship is nearly identical to the starting model in the upper mantle. The only notable change from the starting model is near the top of the lower mantle (Figure 3). The very minor divergence from the starting model in the deep mantle is due to the systematic decrease of δ_S with depth in the lower mantle, approaching a minimum of 1.3 assigned to the D'' layer. In addition, the thermally induced $R_{\rho/S}$ values systematically decrease with depth, further diminishing the influence of variations of $R_{\rho/S}$ on the resulting $R_{P/S}$ values in the deepest parts of the mantle (see equation (4)).

[30] We find velocity-based scaling model correction terms that are highly negative (Table 4) in the cratonic roots reflecting the mass deficiency observed in numerous previous

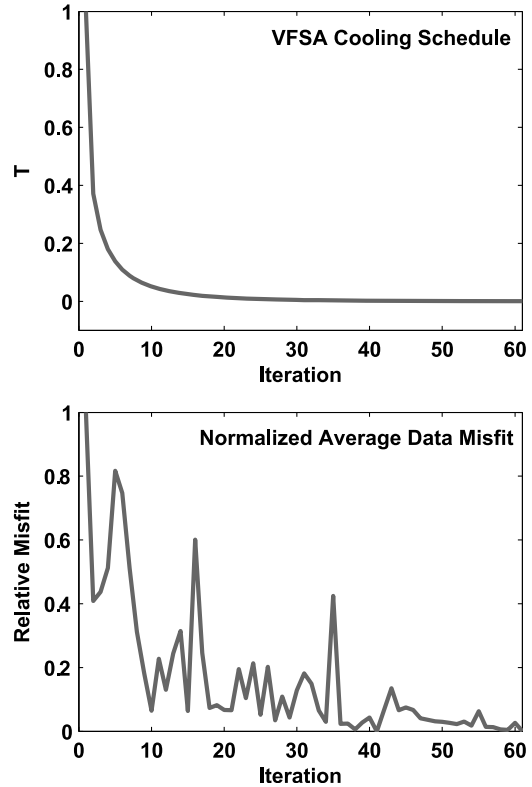


Figure 4. VFSA cooling schedule and data misfit for each accepted scaling model. (top) We chose a rapid cooling schedule since, with each possible set of scaling model parameters, a full-scale nonlinear joint inversion of all seismic and geodynamic data was performed. (bottom) Normalized average data misfit to all data fields for each accepted model update in the VFSA process. Misfits are with respect to joint tomographic models produced with each set of scaling model parameters selected by the optimization procedure. The process was terminated after 61 successful model updates.

studies. In the noncratonic upper mantle, we find positive κ terms, which are in general agreement with the expected behavior due to the temperature dependence of the S wave attenuation parameter (often denoted Q_S) in the upper mantle [Cammarano *et al.*, 2003]. With these scaling model improvements ($R_{\rho/S}^{1-D} \rightarrow R_{\rho/S}^{1.5-D}$ and $R_{P/S}^{1-D} \rightarrow R_{P/S}^{1.5-D}$), we can increase the level of fit to all data sets considered after joint inversion (“GyPSuM_1.5D”; Table 3). The most notable improvement is to the dynamic surface topography field since we are directly accounting for the first-order effects of cratons and other scaling model complexities in the upper mantle, thereby allowing for a greater reconciliation of the free air gravity and dynamic surface topography simultaneously.

5.2. Compositional Decoupling (3-D R Values)

[31] As shown in section 5.1, correcting 1-D R values for cratonic mass depletion and the temperature dependence of Q_S allows for greater reconciliation of the combined set of seismic and geodynamic observations. However, these corrected relationships ($R_{\rho/S}^{1.5-D}$ and $R_{P/S}^{1.5-D}$) do not completely describe the relative behavior of density and wave speeds since we still are not able to fit the seismic data as well as the independently produced models (e.g., TX2008s and P-only in Table 3). The presence of lateral compositional variations is the likely cause for the remaining data misfit, thus requiring 3-D $R_{\rho/S}$ and $R_{P/S}$ values to more adequately explain all of the data simultaneously. We have therefore developed 3-D scaling models through a process we refer to as “compositional decoupling,” since the scaling models are allowed to deviate from the estimated thermal values.

[32] In this iterative process, we allow for slow divergence of the scaling relationships from the 1.5-D values and subsequently update the heterogeneity model through nonlinear joint inversion. We first update $R_{\rho/S}^{3-D}$ through inversion of the geodynamic constraints while assuming a fixed S wave slowness perturbation model determined in the previous step. Similarly, we update $R_{P/S}^{3-D}$ through inversion of P wave information, disregarding the S wave and geodynamic constraints since our goal is to improve the level of fit to the P wave data given an S wave velocity model. The linear systems to be inverted can be represented using the variables defined in Table 2,

$$\begin{aligned} \begin{bmatrix} \mathbf{G}(\Delta\mathbf{m}_S^k) \\ \mathbf{c}(\Delta\mathbf{m}_S^k) \end{bmatrix} R_{\rho/S}^{3-D,k} &= \begin{bmatrix} \mathbf{g} \\ e \end{bmatrix} \xrightarrow{\text{inversion}} R_{\rho/S}^{3-D,k} \\ [\mathbf{L}_P(\Delta\mathbf{m}_S^k)] R_{P/S}^{3-D,k} &= [\mathbf{r}_P] \xrightarrow{\text{inversion}} R_{P/S}^{3-D,k}, \end{aligned} \quad (7)$$

where we have omitted regularization, weighting, and slowness velocity conversion terms for simplicity. At each cycle k , we performed a limited number of LSQR iterations (we chose 4) to restrict the divergence of scaling models from the previous model state. There is no formal basis for the selection of the number of LSQR iterations, but through trial-and-error testing we found that four iterations did not allow the scaling models to move far from the previous state. To complete the k th inversion cycle, we inverted the full system of equations (consisting of all seismic and geodynamic information) for mantle structure assuming the updated $R_{\rho/S}^{3-D}$ and $R_{P/S}^{3-D}$ models, again with a limited number of LSQR iterations. The k th S wave slowness model ($\Delta\mathbf{m}_S^k$) then formed the basis for the subsequent cycle of 3-D scaling model inversions. The pro-

cess was repeated until we observed no significant improvement in the level of fit to all of the data fields considered. Convergence occurred after 64 inversion cycles and the process was thus terminated.

[33] The resulting 3-D scaling model distributions as a function of depth are illustrated in Figure 5. The distribution of $R_{\rho/S}^{3-D}$ values in the shallow upper mantle is broad and biased toward zero, with a substantial number of negative values. This distribution demonstrates lowered scaling factors due to iron depletion in the cold cratonic roots and the temperature dependence of Q_S in the hot noncratonic regions such as the mid-ocean ridges and rift zones. A similar distribution is found in the deepest mantle likely demonstrating significant compositional variations, including within the “superplume” structures [e.g., Ishii and Trampert, 1999; Ritsema *et al.*, 1999; van der Hilst and Káráson, 1999; Masters *et al.*, 2000; Wen, 2001; Ni *et al.*, 2002; Ni and Helmberger, 2003; Trampert *et al.*, 2004; Simmons *et al.*, 2007]. Specifically, the intrinsically high-density material in the superplume structures competes with the thermally induced density anomalies thereby reducing the overall $R_{\rho/S}$ values [Simmons *et al.*, 2007]. The deepest part of the superplume structures could also be intrinsically slow, further lowering $R_{\rho/S}$ values. Aside from the shallow and very deep mantle, we find relatively tight distributions of $R_{\rho/S}^{3-D}$ values with modes similar to the thermal 1-D scaling relationship. We note that, although we find anticorrelation (i.e., negative scaling) of density and S wave velocity in the lower mantle, they are not the dominant signature even in the deepest mantle. Since density and S wave velocity variations are highly sensitive to temperature deviations, it may be argued that the noncratonic mantle shear wave speeds and density variations are primarily temperature driven [Schuberth *et al.*, 2009; Simmons *et al.*, 2009].

[34] The relative heterogeneity ratio (or correlation parameter) $R_{P/S}$ is most often referred to by the inverse ($R_{P/S}^{-1} = R_{S/P}$) in the literature, and a wide range of values have been reported [Vasco *et al.*, 1994; Robertson and Woodhouse, 1996; Su and Dziewonski, 1997; Kennett *et al.*, 1998; Masters *et al.*, 2000; Saltzer *et al.*, 2001; Ritsema and van Heijst, 2002; Antolik *et al.*, 2003]. It has been well established that there are multiple regions in the deep mantle with significant S wave heterogeneities corresponding to very small P wave anomalies. This situation generates nearly unbounded $R_{S/P}$ values and may contribute to the large range of average values reported in the literature. This may in turn lead to discounting thermal variations as a major contributor to seismic anomalies in the lower mantle since the average values often fall well outside the expected thermal bounds [e.g., Karato, 1993; Masters *et al.*, 2000]. For these reasons, we have solved for $R_{P/S}^{3-D}$ in the current study.

[35] Our results show that modes of the distributions of $R_{P/S}^{3-D}$ tend to follow the 1-D component of the VFSA solution ($R_{P/S}^{1.5-D}$) throughout most of the mantle (Figure 5). If we compare these distributions to those generated by models produced solely with the individual seismic data sets (TX2008s and P-only), we find that the joint inversion procedure clearly produces simultaneous P and S wave models more consistent with pure thermal effects. This conclusion is based on the ability to dramatically collapse the distributions of $R_{P/S}^{3-D}$ about the 1-D thermal profile with respect to the independent solutions where the complementary data sets do not constrain one another (Figure 5). However, there are still

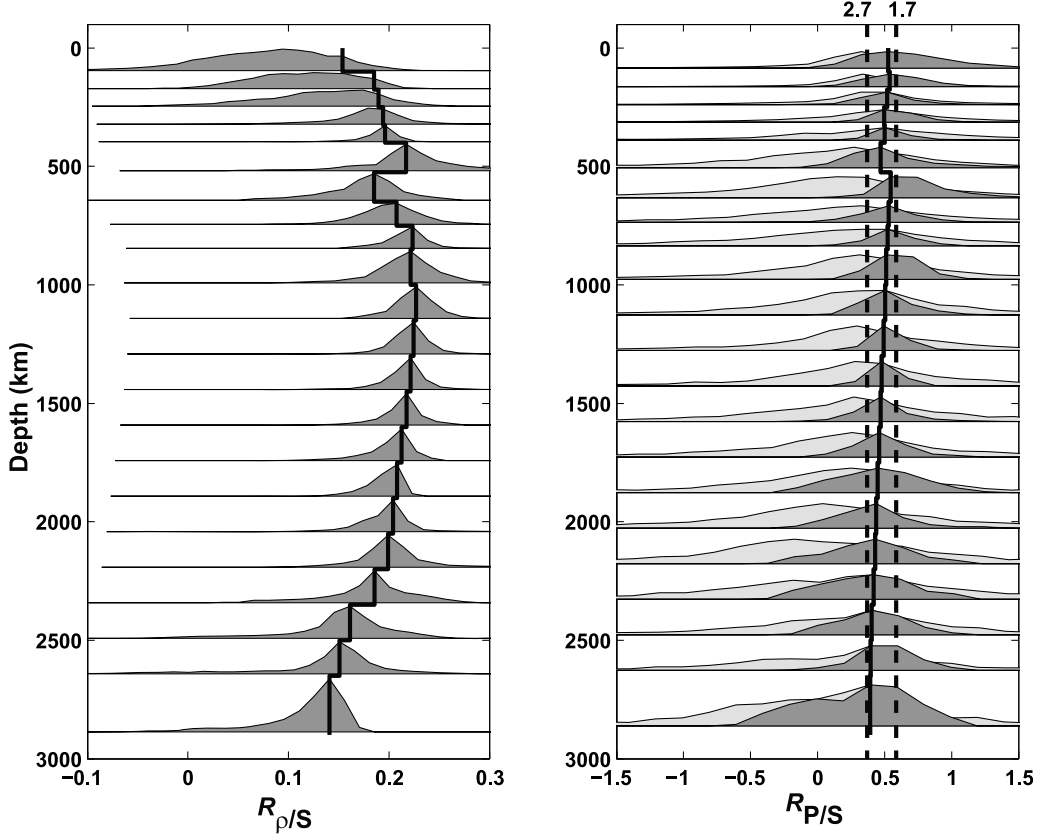


Figure 5. Modeled 3-D scaling factor distributions (dark shaded regions) compared to the 1-D thermal profiles (solid lines) determined with the VFSA optimization procedure. (left) $R_{\rho/S}$ distributions tend to have modes aligning with the inferred 1-D thermal values. The most notable exception is in the shallow upper mantle owing to the compositional signatures of continental cratons. Additionally, distributions are skewed toward zero near the base of the upper mantle and within the deepest mantle. (right) Ratios of P and S wave speed heterogeneity also tend to have distribution modes falling along the inferred 1-D thermal values. The distributions tend to be significantly broader than the density-shear values and are bimodal in the D'' layer. For reference, the dashed lines correspond to $R_{P/S}^{-1} = R_{S/P}$ values of 2.7 and 1.7 as indicated. The distributions of $R_{P/S}$ values were computed for the pure seismic models TX2008s [Simmons et al., 2009] and P-only (this study) for comparison (light gray-shaded areas) to demonstrate the impact of forcing the solution to be more consistent with thermal variations. Note that near-zero $R_{P/S}$ values are a common occurrence in the deep mantle. Therefore, the inverse, $R_{P/S}^{-1} = R_{S/P}$, is unbounded.

some broad scaling model distribution ranges, even though attempts were made to produce a purely thermally driven heterogeneity model in the previous stages. This is most obvious in the deepest mantle where the distributions of $R_{P/S}^{3-D}$ become broad and skewed in some layers. The broad distributions, in part, reflect compositional anomalies in the deep mantle as concluded in numerous previous studies of the relative behavior of mantle properties [e.g., Ishii and Tromp, 1999; van der Hilst and Kárasoñ, 1999; Masters et al., 2000; Saltzer et al., 2001; Trampert et al., 2004].

[36] Relative seismic heterogeneity in the D'' layer appears to be least consistent with thermal variations since a nearly bimodal distribution of $R_{P/S}^{3-D}$ is detected (Figure 5). The primary mode of the distribution (centered near 0.5) could potentially be explained by temperature variations; however, the secondary mode in the distribution (centered near 0) clearly violates the expected thermal behavior in an isochemical mantle [Karato and Karki, 2001]. The decreased

values of $R_{P/S}$ in the D'' layer might be indicative of pressure-induced phase changes to postperovskite (pPv), creating a partial decorrelation of P and S wave heterogeneity [Murakami et al., 2004; Oganov and Ono, 2004; Iitaka et al., 2004; Tsuchiya et al., 2004; Wookey et al., 2005; Hirose, 2006; Hernlund and Houser, 2008; Hutko et al., 2008]. This hypothesis is based on mineral physics analyses that indicate that shear modulus increases while bulk modulus is relatively unchanged due to the transition to the pPv phase [e.g., Tsuchiya et al., 2004]. Moreover, the large spread of relative heterogeneity values near zero may be due to patchy occurrences of pPv (and perhaps lens-like seams) modulated by the background temperature [Hernlund et al., 2005; Lay et al., 2006; Hernlund and Houser, 2008]. The discrepancy between the distributions of P and S wave anomalies in the deep mantle is robust [Hernlund and Houser, 2008] and persists after performing a joint inversion designed to reduce these effects. However, we point out that the joint inversion

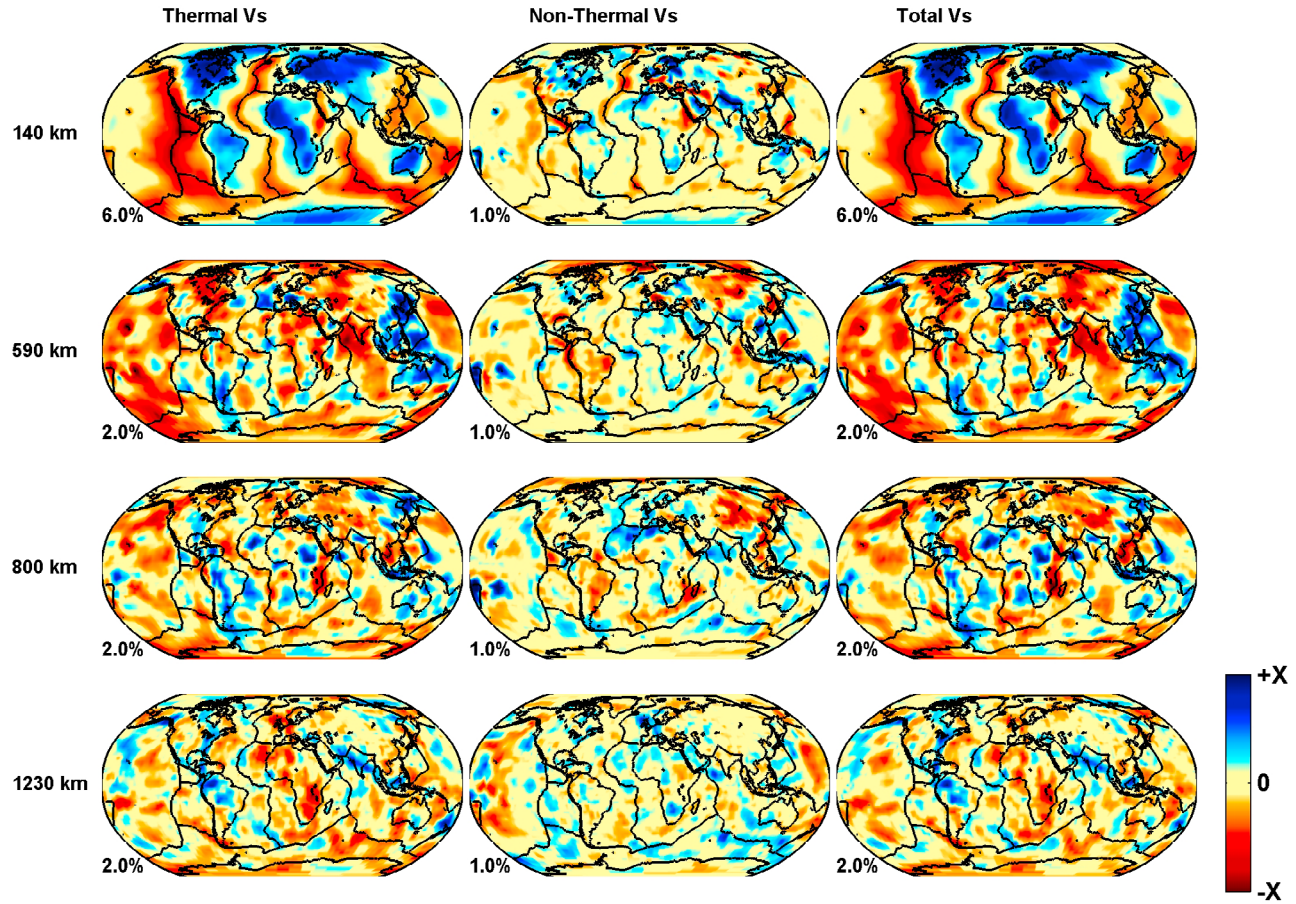


Figure 6. (a) S wave velocity perturbations in the GyPSuM model. Each row corresponds to a particular depth, and the three columns correspond to each component of the velocity field. The “total” field is simply the sum of “thermal” and “nonthermal” components defined in the text. The “Nonthermal” heterogeneity levels are significantly smaller than the thermal signatures in the upper half of the mantle. Note that the color scales change for each frame according to the amplitude (X) printed in the bottom left corner of each frame. (b) Linear fast zones attributed to past subduction beneath North America and southern Eurasia/India persist to at least 1800 km depth. Low-velocity zones dominate much of the deep mantle shear wave heterogeneity and are most evident in the African and Pacific superplume structures. High-velocity zones in the D'' layer generally occur beneath regions where subduction has occurred since the past supercontinent cycle [Anderson, 2002], suggesting that slabs eventually reach the base of the mantle.

process in this study leads to seismic anomalies more consistent with thermal variations as manifested through the distribution of $R_{P/S}$ (Figure 5).

6. GyPSuM Model

6.1. Thermal and Nonthermal Contributions

[37] The final model, GyPSuM, is illustrated in Figures 6a, 6b, 8a, 8b, 9a, and 9b. The inversion procedures described within this report allow for the estimation of what we refer to as “thermal” and “nonthermal” contributions to mantle heterogeneity. The “thermal” contributions to each of the model fields (velocities and density) are estimated from the joint inversion results obtained by employing the temperature-induced part of the optimum 1.5-D scaling model. The “nonthermal” contributions are computed by subtracting the thermal components from the final model developed in the previous section. Therefore, the nonthermal heterogeneity

field may be thought of as a residual field required in addition to the thermal field in order to fit the data. It should be noted that there is a probability that some of the signatures we refer to as “nonthermal” might actually be due to the effects of laterally varying Q_S since, in the development of the 1.5-D scaling model, we only considered first-order thermal scaling corrections in the upper mantle and no systematic corrections in the lower mantle (see section 5.1).

[38] In the upper mantle, we find mostly minor nonthermal contributions to the S wave velocity heterogeneity field (Figure 6a). Some of the most prominent nonthermal contributions to the S wave heterogeneity field are found in the deep mantle within the superplume structures (most notably beneath Africa; Figure 6b). Our results imply that these superplume structures are intrinsically slow in terms of S wave speeds lending support to the idea that these features are partially produced by the sweeping of intrinsically dense material into regions of large-scale upwelling mantle

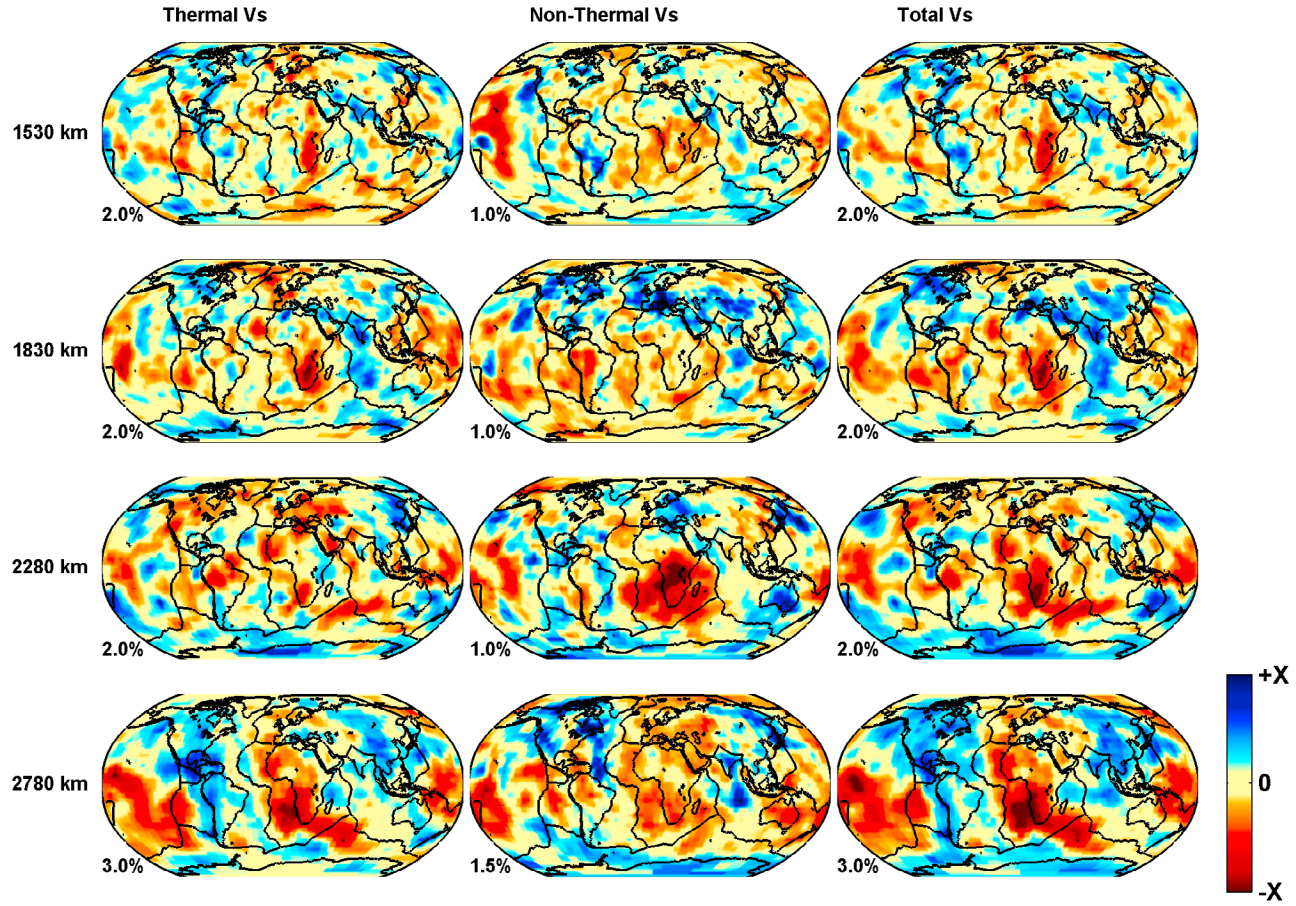


Figure 6. (continued)

[McNamara and Zhong, 2005]. Specifically, near 2280 km depth (Figure 6b), we find significant low-velocity S wave signatures in the “nonthermal” field within the African superplume structure. This apparent nonthermal signature manifests itself through the modeled decrease of $R_{\rho/S}$ found through the 3-D scaling model inversion process relative to the 1-D scaling profile (i.e., thermal profile). Our inferred nonthermal (or compositional) signature within these superplumes (notably under Africa) may be explained in terms of iron enrichment, since this will produce a reduction in S wave speed in addition to the reductions expected for increased temperature [e.g., Forte and Mitrovica, 2001]. Alternatively, a similar effect may be expected due to increased temperatures and the impact to Q_S [Karato and Karki, 2001].

[39] Although there are apparent nonthermal influences on the shear velocity field, temperature variations appear to be the dominant factor. This is demonstrated more quantitatively through the calculation of the root mean square (RMS) amplitudes of the individual thermal/nonthermal heterogeneity fields (Figure 7). We find that the RMS amplitude of the thermally induced S wave heterogeneity is the largest contributor to the overall field throughout the entire mantle. This result is in direct agreement with Quéré and Forte [2006] and Schubert et al. [2009], who found that steep lateral temperature gradients could mostly account for the large-scale, low-velocity superplume structures beneath Africa and the Pacific Ocean.

[40] Density heterogeneity in the shallow upper mantle is produced by both temperature and compositional variations (Figure 8a). As expected, the thermal signature in the cratonic regions is high density due to decreased temperatures, while the compositional signature is low density due to depletion of basaltic components. Because of the temperature dependence of Q_S , the thermal signatures have higher amplitude in seismically fast (cold) regions than in slow (hot) regions. However, the competing thermal/compositional effects in the cratonic regions produce far lower amplitude densities in the cratons overall, relative to the purely thermally induced density field (Figure 8a).

[41] Compositional density anomalies are small relative to thermally driven density field throughout most of the non-cratonic mantle based on the RMS amplitude calculations (Figure 7). However, in the bottom ~400 km of the mantle, the compositional influence increases dramatically. The major contributions to the compositional density fields are within the African and Pacific superplume structures. The central cores of these features are found to be intrinsically dense. The positive intrinsic density of these structures offsets the thermally driven density in portions of the superplume structures, thereby reducing the overall buoyancy similar to the results of Simmons et al. [2007, 2009]. However, the amplitudes of the nonthermal high-density signatures in the superplumes are larger in the GyPSuM model relative to TX2007 [Simmons et al., 2007] and TX2008 [Simmons et al., 2009].

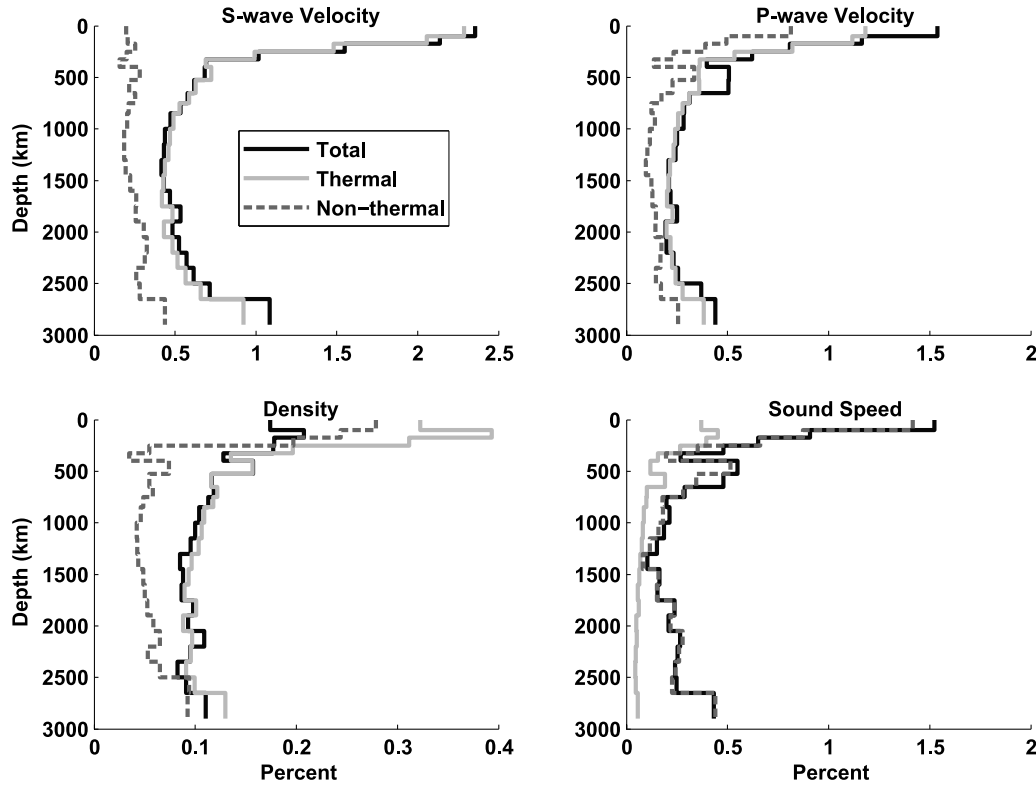


Figure 7. Root mean square (RMS) amplitudes of wave speeds and density. Each field is separated into thermal and nonthermal contributions, and RMS amplitudes are subsequently computed. *S* wave heterogeneity is dominantly produced by variations in temperature throughout the mantle. *P* wave heterogeneity is also largely controlled by variations in temperature, but to a lesser degree than shear waves. Similarly, thermally induced density anomalies are typically larger than compositionally induced heterogeneity. However, we find substantial opposing compositional anomalies associated with the mass-depleted cratons and the intrinsically dense superplume structures. These anomalies produce a level of compositional influence that rivals the thermally driven density heterogeneity in the shallowest and deepest mantles. Sound speed heterogeneity is dominated by compositional variations throughout most of the mantle. The low amplitude of the thermally induced sound speed heterogeneity in the deep mantle is a result of δ_S values approaching 1 (see text). Therefore, the relative behaviors of bulk modulus and density are very similar in the presence of temperature variations in the lower mantle providing very small sound speed variations.

Moreover, the net result of the combined thermal and non-thermal density anomalies is overall positive density anomalies in some parts of the African superplume structure, most notably within the D'' layer (Figure 8b). This significant difference from TX2007 and TX2008 is a direct product of the addition of the *P* wave constraints that are sensitive to *P* wave velocity but related to *S* wave velocity and density through scaling relationships. The introduction of *P* wave data yields a joint set of constraints that more tightly limit the ability of thermally induced heterogeneity models to simultaneously explain the combined set of data. Given the increased difficulty of satisfying the data with a pure thermally induced heterogeneity model, the *P* wave constraints effectively increase the level of compositional influence required and the net result is high-density anomalies at the base of the African superplume.

[42] Studies utilizing normal mode splitting functions [e.g., Ishii and Tromp, 1999; Trampert et al., 2004] have found overall high densities in these deep mantle structures. Our results differ in that the high-density material observed in these features is far more localized and has much lower

amplitude than in the previous studies. The discrepancy may be explained by the study of Kuo and Romanowicz [2002] that suggested that density anomalies resulting from normal mode data are subject to contamination of *P* and *S* wave velocity structure into density structure (see section 7 for more on this topic).

[43] *P* wave heterogeneity is shown to have significantly more influence from compositional variations relative to *S* wave velocity (Figures 9a and 9b). These signatures are most notable in the cratonic regions, which are known to be compositionally heterogeneous (Figure 9a). We also detect significant compositional anomalies throughout the lower mantle that are typically half of the amplitude of the thermally induced anomalies. One of the more notable nonthermal *P* wave velocity signatures in the deep mantle are negative values associated with the subducted Farallon and Tethys slabs below ~ 1500 km depth (see Figure 9b at 1830 km depth). These negative nonthermal signatures oppose the thermal signatures (fast) and act to mask the overall *P* wave signatures of the deepest extent of the ancient subducted slabs. It is therefore apparent that compositional variations

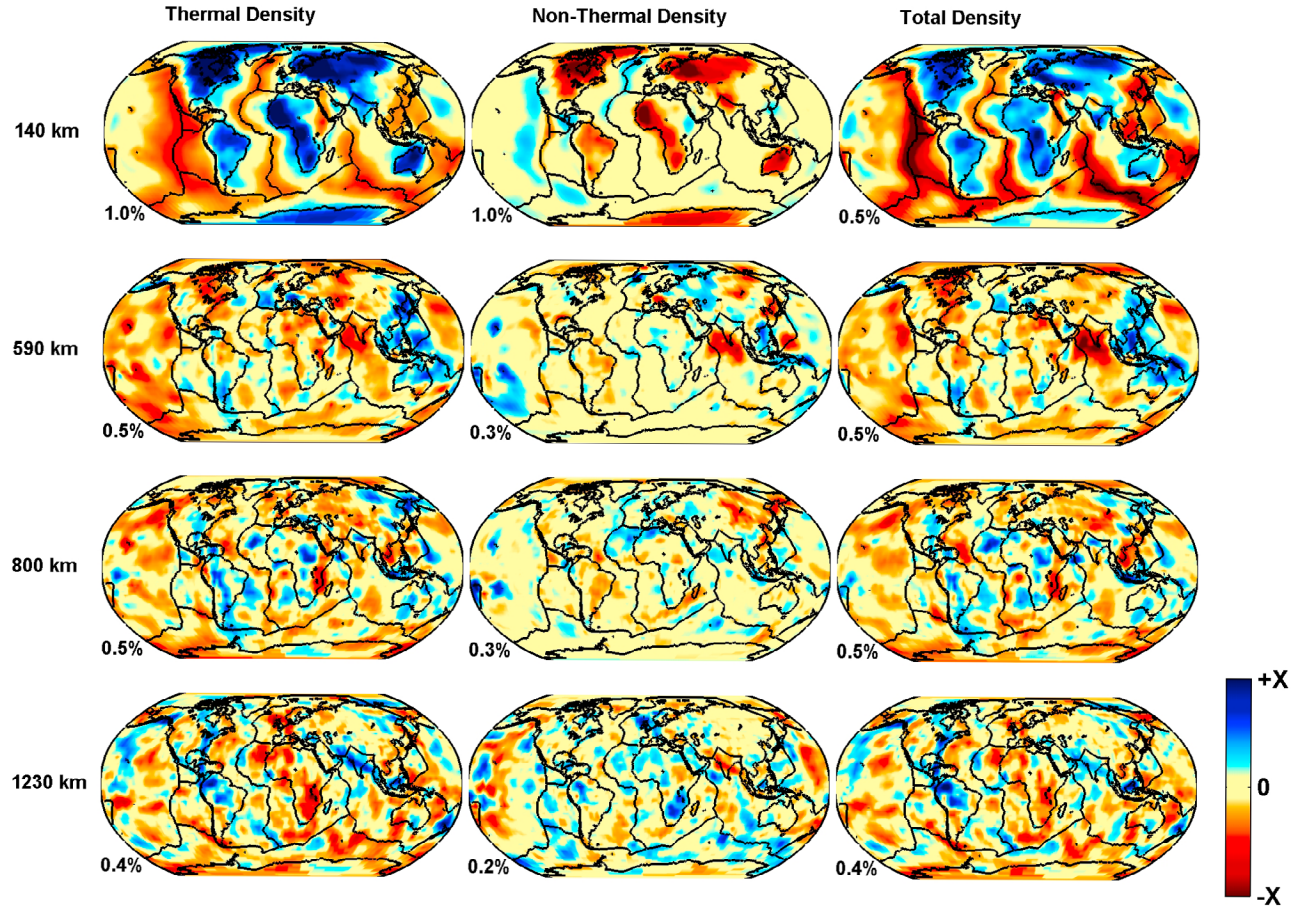


Figure 8. (a) Density perturbations in the GyPSuM model. The thermally induced high-density signatures in the cratonic roots are offset by the nonthermal contributions severely reducing the amplitude of the overall negative buoyancies. Outside of the cratons, upper mantle density structure is dominated by the effects of temperature variations. (b) The primary nonthermal contributions to the density field are within the deepest portion of the superplume structures. The central cores of these structures are intrinsically dense, offsetting the effects of temperature. In some localized zones within the superplumes, we find near neutral buoyancies and mild negative buoyancies, which may account for the stabilization of these structures over long time scales.

contribute significantly to P wave heterogeneity; yet the RMS amplitudes of the individual thermal/nonthermal structures suggest that temperature variations are most often the largest contributor.

[44] We have examined this result further by computing bulk sound speed variations from the modeled P and S wave anomalies and similarly computed the RMS amplitudes as a function of depth (Figure 7). We find that the primary contributor to sound speed heterogeneity is variations in composition rather than temperature. This finding provides strong support to the initial results by Forte and Mitrovica [2001] that showed that bulk sound speed anomalies provide an effective mapping of compositional heterogeneity in the deep mantle. This is especially apparent in deep mantle where the sensitivity of sound speed to temperature is weak due to δ_S values approaching 1 (see equation (3)). However, the considerable effect of temperature on the relative behavior of shear modulus and density produces P wave anomalies that are largely controlled by thermal variations. The dominant thermal control explains the reason for well-correlated S and P wave anomalies, while sound speed is often poorly correlated with

S wave speeds [Su and Dziewonski, 1997; Masters et al., 2000; Kennett and Gorbatov, 2004].

6.2. Wave Speed and Density Correlation

[45] On the basis of the RMS amplitudes of wave speeds and density heterogeneities (Figure 7), we may conclude that temperature variations are the primary cause of mantle heterogeneity. We also find that the correlation of S wave velocity and the other modeled fields are highly positive in the majority of the mantle (Figure 10). In particular, the correlation coefficient of density and S wave speeds approaches 1 in a large portion of the mantle. This correlation drops in the deepest mantle owing to the compositional anomalies associated with the superplume structures. Similarly, P and S wave heterogeneities are highly correlated when all anomalies (estimated thermal and nonthermal contributions) are considered. This result, along with the systematic decorrelation of sound and shear speeds with depth, is generally consistent with past results [e.g., Masters et al., 2000; Saltzer et al., 2001].

[46] Sound and shear speeds become anticorrelated in the deep mantle with a negative peak just below ~ 2000 km depth,

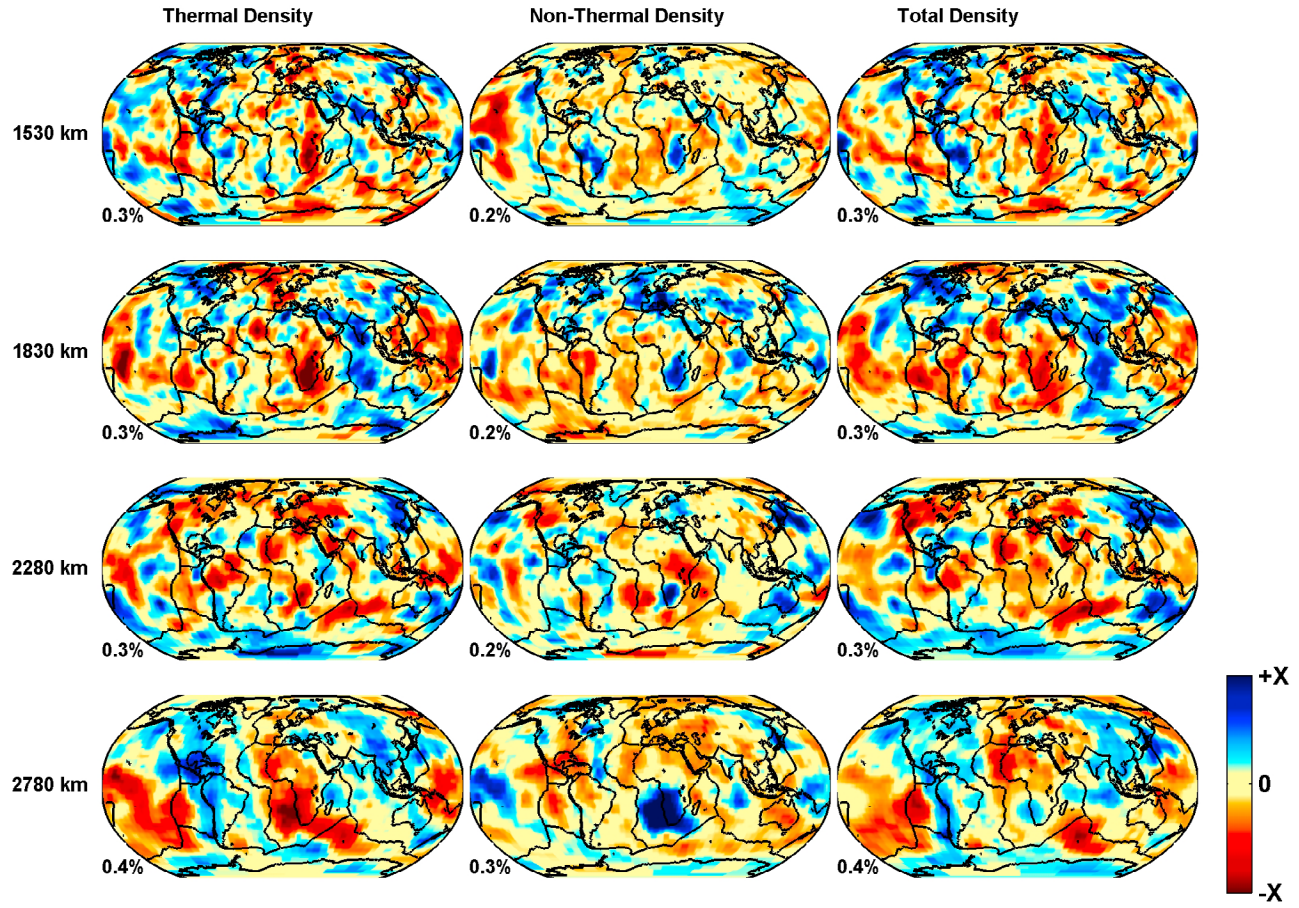


Figure 8. (continued)

a result that is also similar to the results presented by *Saltzer et al.* [2001]. However, just above the D'' layer, the correlation jumps to positive values and then quickly returns to negative within the D'' layer unlike the aforementioned study. Both *Saltzer et al.* [2001] and *Masters et al.* [2000] show hints of this cyclical correlation behavior, but the amplitude of the correlation jumps presented in the current study are more dramatic. This correlation behavior may imply the existence of two distinct depth zones with elevated compositional influence centered at ~ 2000 km depth and within the D'' layer. The layer immediately above D'' would then represent a transitional layer that is more strongly controlled by temperature variations. This argument may have merit given the elevated compositional sensitivity of sound speed in the deep mantle (see Figure 7). However, we are reluctant to draw definitive conclusions from this observation alone since other mechanisms such as the pPv phase transition could contribute to the pattern. Additionally, the correlation jump occurs over a single model layer and is possibly an artifact of parameterization.

[47] Although the modeled P/S wave speeds and density are mostly correlated when all anomalies are considered in the calculation, separating the fields according to fast and slow S wave anomalies reveals more complicated results (Figure 10). In particular, the correlation of slow S wave structures and density are much smaller (sometimes negative) in the deep mantle. The primary source of this deep mantle decorrelation is easily recognized to be the effects of the opposing thermal/

compositional density signatures associated with the superplume structures (Figure 8b).

[48] The correlation of slow S wave anomalies and the corresponding P wave anomalies is high, similar to the total correlation. However, if we compute the correlation of fast shear velocity zones with the corresponding P wave anomalies, we find a dramatically different result (Figure 10). Specifically, P wave anomalies in regions with fast S wave velocities systematically decorrelate with depth beginning at ~ 1500 km and peaking to slightly negative values at ~ 2100 km depth. Thus, the deep mantle high shear velocity zones, which may be attributed to ancient subducted slab remnants, have significantly different geographic patterns than the P wave anomalies due to strong anticorrelation of shear and sound speeds. In extreme cases, the high-velocity shear zones correspond to low-velocity P wave anomalies. Therefore, the thermal P wave signatures are significantly countered by the “nonthermal” component (see Figure 9b; 1830 km depth) producing muted or absent total P wave structure where S wave velocities are fast and densities are high. It is unclear if the deep mantle fast shear velocity blobs are remnant slab materials. But it is evident that these features have very different P wave signatures that do not adhere to their expected thermal behavior, differing from zones with low shear velocity in the lower half of the mantle.

[49] As pointed out by *Boschi et al.* [2007], deep lower mantle anomalies are dominated by negative velocities at low

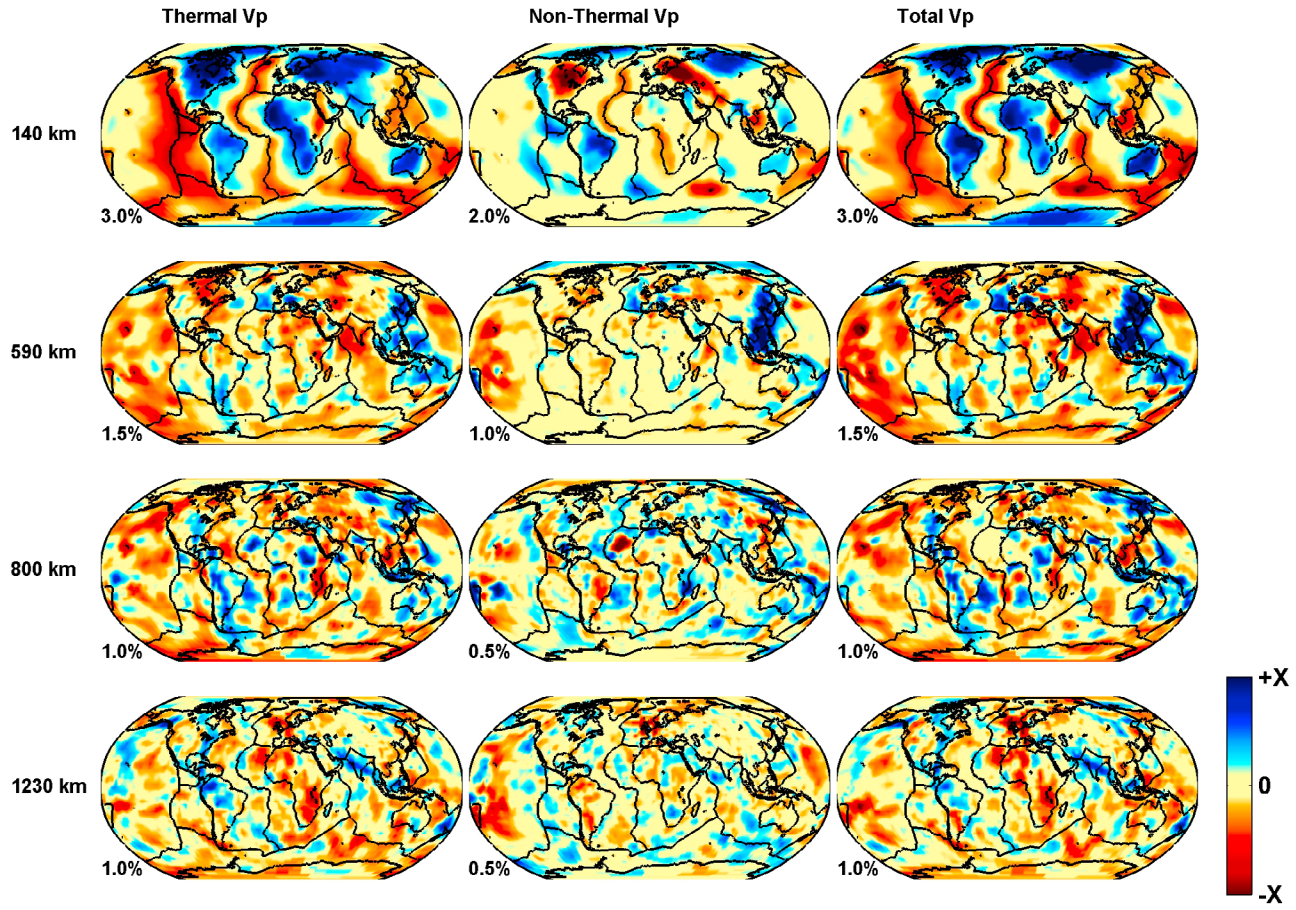


Figure 9. (a) P wave velocity perturbations in the GyPSuM model. P wave heterogeneity in the shallow upper mantle is strongly influenced by compositional variations. This is most significant in cratonic regions, but other scattered nonthermal anomalies are also evident. (b) Nonthermal influences on P wave heterogeneity are significant in the lower half of the mantle. Most notably, the thermally induced high-velocity zones are effectively muted by opposing low-velocity signatures. In contrast, the patterns of the low-velocity regions in the total field generally match the thermally induced field. This behavior may be due to compositional variations and/or the effect of electronic spin transitions (see text for a discussion).

spatial frequencies. On the other hand, high-velocity anomalies in the lower mantle are typically restricted to high spatial frequencies that may not be well resolved in some cases. Correlation properties of fast shear anomalies in the lower mantle, based on independently derived P and S wave models, would therefore be dubious. However, in the development of the GyPSuM model, both P and S wave data were modeled simultaneously with the same parameterization and regularization mitigating a number of issues including the varying resolution of each data set.

6.3. Compatibility With Geodynamic Constraints

[50] We finally consider the extent to which the 3-D density anomalies in GyPSuM, identified by “Total Density” in Figures 8a and 8b, is able to reproduce the geodynamic constraints illustrated in Figure 1. We carried out a mantle flow calculation employing these density anomalies and using the radial viscosity profile in Figure 2a that was previously derived by Mitrovica and Forte [2004]. A comparison of the predicted dynamic surface topography (Figure 11b) and the corresponding crust-corrected surface topography

(Figure 11a) shows a very good global fit, quantified in Table 3 (final row).

[51] The comparison of predicted and observed free air gravity anomalies (Figures 11c and 11d) also shows excellent agreement (quantified by the final row in Table 3). The almost equivalent fits to both the surface topography and gravity anomalies resolve a longstanding debate concerning the ability of the tomography-based mantle flow models to reconcile both data sets [e.g., Forte et al., 1993; Le Stunff and Ricard, 1995; Forte, 2007].

[52] The predicted tectonic plate motions driven by the total density anomalies in the 3-D GyPSuM model are quantified (last row in Table 3) in terms of the fit to observed horizontal divergence field. The match is nearly perfect (99% variance reduction), and it is therefore of interest to determine the extent to which the predicted radial vorticity matches that of the NUVEL-1 motions in the NNR frame. As discussed previously (section 2), the radial vorticity may be mathematically regarded as a linear mapping of the horizontal divergence for a given (fixed) plate geometry. We find that the predicted radial vorticity field yields a 95% fit (variance

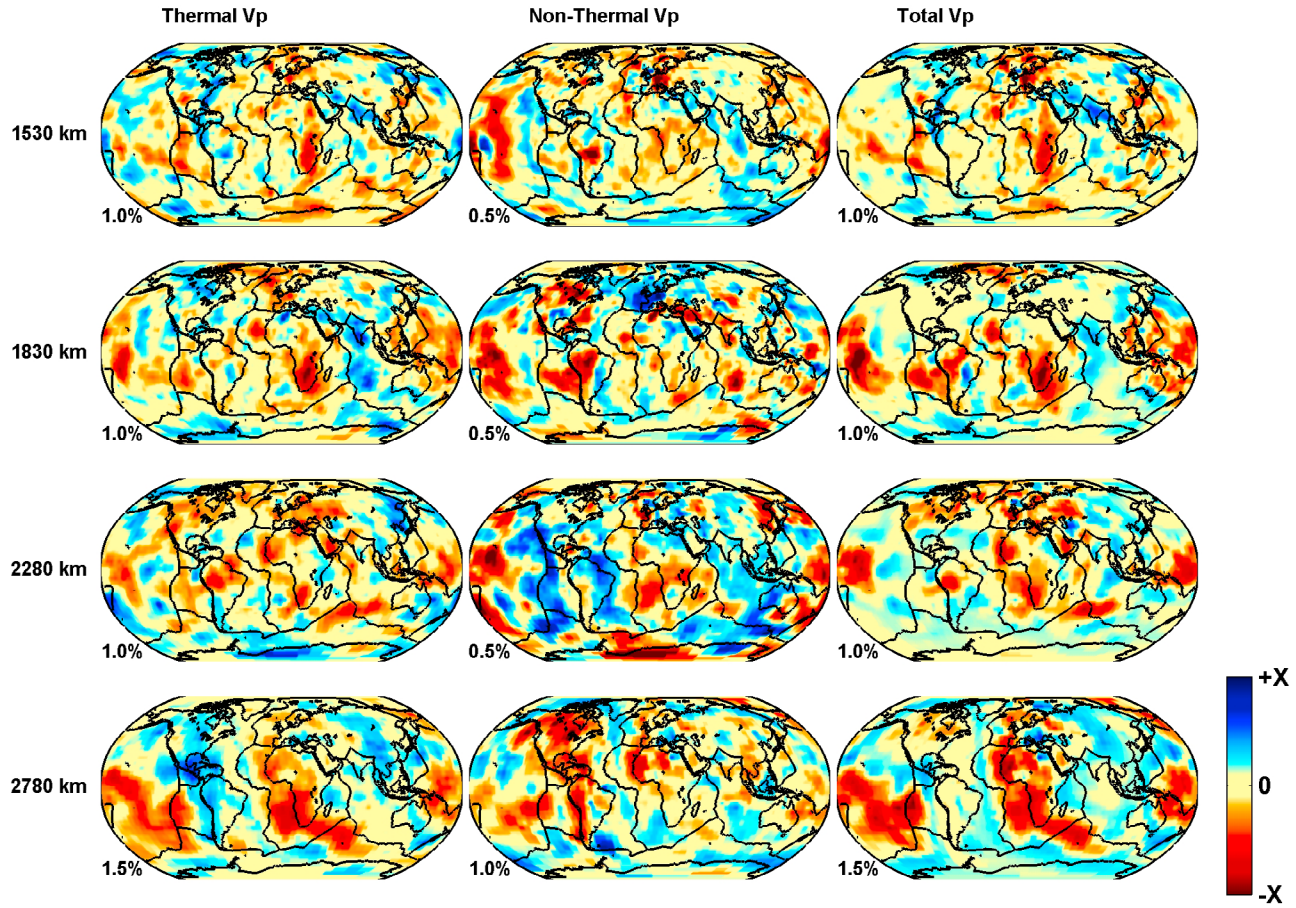


Figure 9. (continued)

reduction) to the observed NUVEL-1-NNR radial vorticity field.

7. Discussion

[53] Wave speeds and density are highly correlated throughout most of the mantle when all anomalies are considered (Figure 10). However, fast shear velocity zones and the corresponding P wave anomalies systematically decorrelate in the $\sim 1500\text{--}2500$ km depth range, suggesting another mechanism besides simple thermal variations. The combined thermal and other possible mechanism(s) mute P wave velocity signatures in zones commonly interpreted as subducted slabs in the deep mantle on the basis of S wave tomographic solutions that show persistent fast anomalies at these depths (compare the “total” V_S and V_P fields in Figures 6b and 9b at 1830 km depth). A possible explanation for the P and S wave discrepancies is the effect of electronic spin transitions in iron-bearing minerals. Studies of the elastic effect of electronic spin transition suggest that, at midmantle depths, the transition will generate negative seismic velocity anomalies over a broad depth range [e.g., *Crowhurst et al.*, 2009; *Wentzcovitch et al.*, 2009]. The effect of this mechanism would then oppose the thermally induced fast velocity signatures within the subducted slab material. Moreover, if the temperature decrease is small enough, the effects of spin transitions could overwhelm the thermally induced high P wave velocities,

thereby muting out the structure entirely. The S wave signatures in the supposed subducted slab remnants could remain fast given the relatively increased sensitivity of S wave velocity to thermal variations. In such a scenario, the high-temperature zones (producing low-velocity signatures) would remain slow since the combined effects of increased temperature and spin transition would be constructive. Therefore, the correlation of low shear velocity zones with the corresponding P wave values would remain large and positive.

[54] One potential problem with the hypothesis stated above is the fast, nonthermal S wave speeds we estimate in these zones (Figure 6b; 1830 km depth). If the previous scenario were true, we would expect an opposite (slow) nonthermal shear velocity signature. A possible explanation for this apparent fast nonthermal anomaly is the underestimation of the thermal contributions to the S wave velocity field in this depth range. The joint inversion with thermal scaling relationships (1-D in the lower mantle) incorporated both S and P wave data that conflict when scaled in this simplified way as evidenced by our results. Thus the thermal S wave heterogeneity solution could have been corrupted by the P wave data that require nearly no anomalies in these subducted slab remnants. Nonetheless, we find that zones with fast S wave speeds (centered at ~ 2000 km depth) correlate poorly with the corresponding P wave anomalies in the total velocity fields (Figure 10) and are often muted and/or absent (compare Figures 6b and 9b). Spin transitions

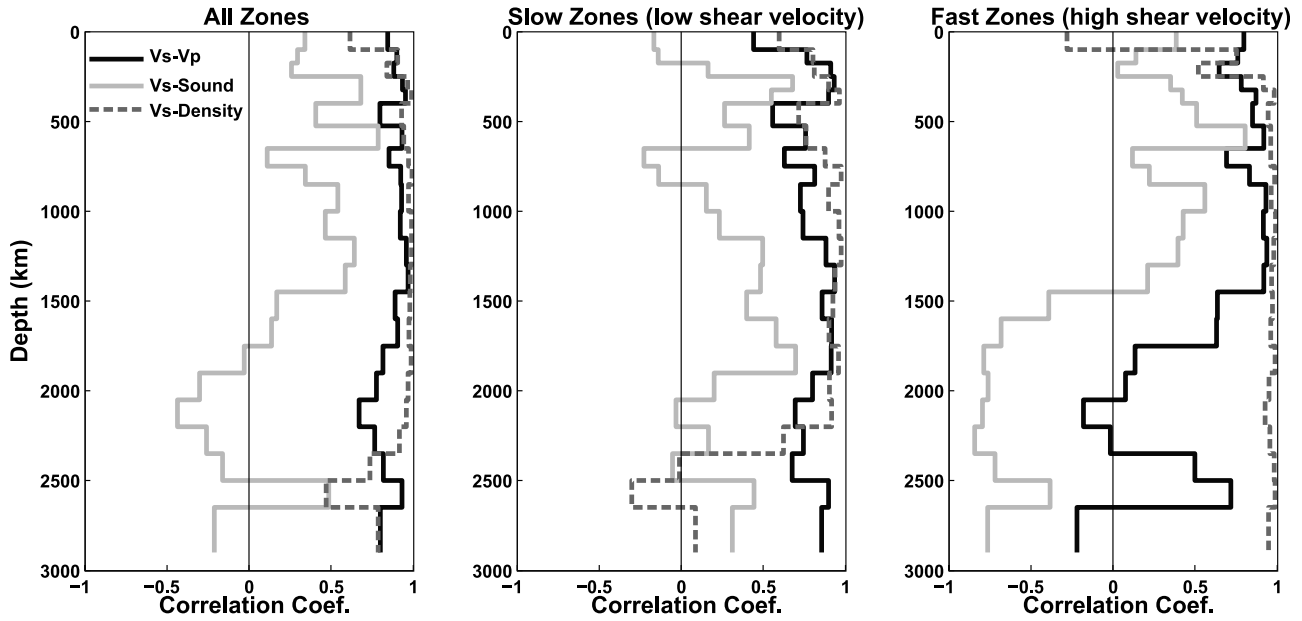


Figure 10. Depth-dependent correlation of S wave heterogeneity and other modeled properties. (left) Correlation coefficients with all heterogeneity considered. S and P wave velocities tend to be highly correlated throughout the mantle ($Vs\text{-}Vp$). Similarly, density and S wave velocity perturbations are positively correlated throughout the mantle ($Vs\text{-}Density$). However, sound speed is often decorrelated or mildly anticorrelated with S wave heterogeneity ($Vs\text{-}Sound$). (center) Correlation based on low S wave velocity regionalization. When we consider only the low shear velocity structures in the correlation measurement, we find that P wave anomalies corresponding to these zones remain fairly well correlated. However, density heterogeneity systematically decorrelates with shear speed in the deepest mantle primarily owing to the intrinsically dense material within the superplume structures. (right) Correlation based on high S wave velocity regionalization. Fast shear velocity structure is highly correlated with density throughout the lower mantle. Correlation of fast S wave zones in the deep mantle (>1500 km depth) with the corresponding P wave anomalies decreases, suggesting a systematic departure from simplified thermal effects in ancient subducted slab anomalies (see text for discussion).

potentially explain our observations, but the actual effects that electronic spin transitions have on mantle materials is still uncertain [see *Badro et al.*, 2003, 2004; *Hofmeister*, 2006; *Lin et al.*, 2007, 2008; *Speziale et al.*, 2007; *Stackhouse et al.*, 2007; *McCammon et al.*, 2008; *Crowhurst et al.*, 2009; *Wentzcovitch et al.*, 2009].

[55] Aside from the discrepancies of wave speeds in the ancient subducted slab remnants, the superplume structures beneath Africa and the Pacific Ocean possess properties that cannot be explained by temperature variations alone. Most notably, portions of the superplume structures have significant positive nonthermal density signatures that are relatively broad in the D'' layer and extend upward through the midmantle with a more narrow lateral extent (Figure 8b). These density signatures are interpreted as intrinsically dense material that is partially entrained within the upwelling superplumes [*Simmons et al.*, 2007]. The intrinsic density of this material counters the thermally induced density, thereby reducing the overall buoyancy of the upwellings [see *Simmons et al.*, 2007, 2009; *Forte et al.*, 2010]. The amplitude of the nonthermal high-density signatures in the superplumes are larger than our previous tomography results [*Simmons et al.*, 2007, 2009] owing to the addition of the P wave constraints that help limit the range of possible configurations of density heterogeneity in the joint inversion process.

[56] Combining the thermal and nonthermal components of the density field, we find overall positive density anomalies within the South Africa superplume structure. Studies incorporating normal mode splitting functions have similarly modeled high-density signatures in the low-velocity superplume structures [e.g., *Ishii and Tromp*, 1999; *Trampert et al.*, 2004], suggesting a dominant compositional influence on the heterogeneity in these regions. However, our results differ strongly in that the overall high-density zones appear to be far more localized and have lower amplitude. Specifically, we find only slightly positive density anomalies beneath the extreme southern tip of Africa that is mostly confined to the D'' layer. Beneath the Pacific Ocean, we find no significant positive density anomalies in the low-velocity structures. However, a localized portion of the Pacific superplume density structure is strongly affected by the positive intrinsic density of the material, also muting the temperature-induced buoyancy.

[57] Similar to the results of *Kuo and Romanowicz* [2002], our results suggest that mantle density models developed with normal mode data [e.g., *Ishii and Tromp*, 1999; *Trampert et al.*, 2004] may be overestimating the amplitudes and scale lengths of high-density anomalies at the base of the superplume structures. Moreover, *Kuo and Romanowicz* [2002] suggest that up to 0.5% density anomalies could be obscured in normal mode data and that either high or low

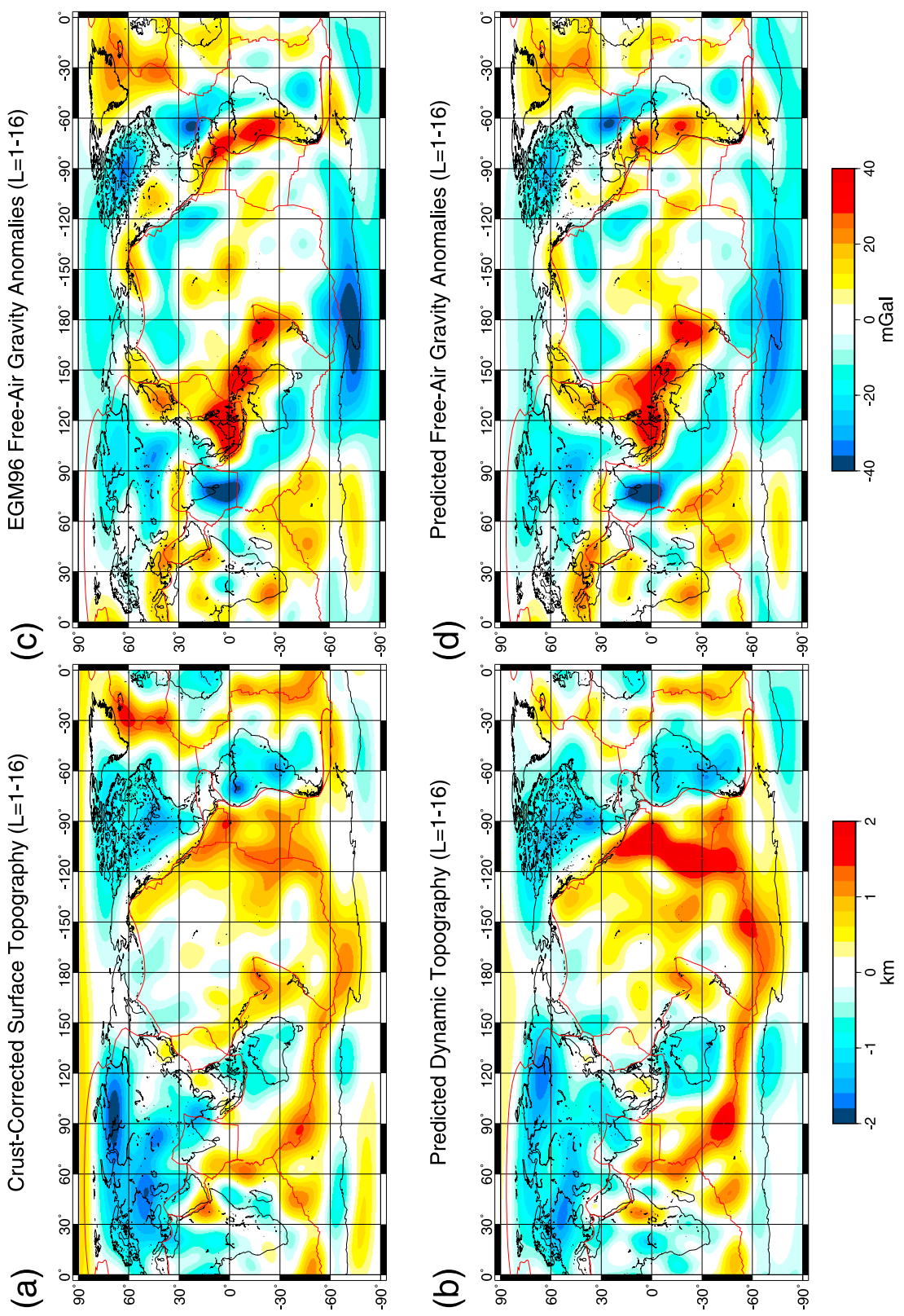


Figure 11. Comparison of observed and predicted convection-related observables. (a) The crust-corrected surface topography from Figure 1c. (b) The dynamic topography predicted with the tomography-based mantle flow model. (c) The observed free air gravity anomalies from Figure 1b. (d) The free air gravity predicted with the tomography-based mantle flow model. The mantle flow calculations employ the radial viscosity profile in Figure 2a and the density anomalies from the final joint seismic-geodynamic inversion with a fully 3-D density–velocity scaling. All fields have been expanded in spherical harmonics up to degree and order 16.

densities could be modeled in the superplume structures, depending on starting conditions of the inversion. We cannot exclude the possibility of intense and broad high-density anomalies within the superplume structures in the current study. However, we can conclude that there is no requirement for extensive zones of high-amplitude positive density anomalies in the superplume structures to simultaneously explain all the geodynamic and seismic constraints we have employed.

8. Conclusions

[58] We have constructed a tomographic model of mantle *S* wave speeds, *P* wave speeds, and density through the simultaneous inversion of seismic and geodynamic observations. The mantle model (labeled GyPSuM) was constructed with the underlying hypothesis that temperature variations are the dominant cause of mantle heterogeneity via the integration of mineral physics parameters that describe the relative behavior of mantle properties due to thermal effects. Thus, GyPSuM represents the “simplest” model of the mantle, whereby only the minimal amount of compositional heterogeneity is introduced to satisfy *P* and *S* wave travel time data as well as the global free air gravity field, dynamic surface topography, and the divergence of the tectonic plate velocities. Thermal dominance of heterogeneity is best demonstrated through the calculated RMS amplitudes of the estimated thermal and nonthermal contributions to the model fields (wave speeds and density) shown in Figure 7.

[59] Overall, we find that *P* wave, *S* wave, and density anomalies may be primarily attributed to variations in temperature. However, substantial chemical heterogeneity is required in the cratonic roots of continents and, to a lesser extent, in the deepest mantle. In particular, we find positive density anomalies at the base of the African superplume structure. This high-density zone is more localized and has much lower amplitude than the zones observed in density models produced with normal mode data [e.g., *Ishii and Tromp*, 1999; *Trampert et al.*, 2004], which are subject to considerable nonuniqueness [*Kuo and Romanowicz*, 2002]. Another intriguing observation from GyPSuM is the systematic decorrelation of fast shear velocity zones and the corresponding *P* wave anomalies in the ~1500–2500 km depth range. This observation may suggest another mechanism besides simple thermal variations for the generation of midmantle heterogeneity. We argue that a possible explanation for the *P* and *S* wave decorrelation is the effect of electronic spin transitions in iron-bearing minerals, which may mask the overall *P* wave signatures of ancient subducted slabs in the deep mantle.

[60] It should be noted that we assumed raypaths (infinite frequency approximation) and that considering finite frequency effects could alter the results of this study. Studies considering finite frequency effects have shown that the amplitude of low-velocity anomalies could be considerably larger than those produced by ray theory [*Montelli et al.*, 2004; *V. Lekić and B. Romanowicz*, Inferring mantle structure by full waveform tomography using spectral element method, submitted to *Geophysical Journal International*, 2010]. These amplitude differences might be significant to the study presented herein, but direct comparisons of ray and finite frequency theories provide evidence that the basic arrangement of mantle heterogeneity does not dramatically

change [*Boschi et al.*, 2006; *Peter et al.*, 2009]. Incorporation of more data and data types may result in models that require stronger chemical heterogeneity in the future. Resolving the issue of chemical versus thermal causes for observed heterogeneity will also require the incorporation of more comprehensive and stricter mineral physics constraints.

[61] **Acknowledgments.** We thank Barbara Romanowicz and an anonymous reviewer for their constructive comments that helped improve our paper. We also acknowledge helpful discussions with Steve Myers, Elise Knittle, and Jung-Fu Lin. A.M.F. wishes to acknowledge funding from the Canadian Institute for Advanced Research, NSERC, and from the Canada Research Chair program. L.B. wishes to thank Domenico Giardini for his constant support and encouragement. S.P.G. thanks the Jackson School of Geosciences at the University of Texas for their support. This work performed under the auspices of the U.S. Department of Energy by Lawrence Livermore National Laboratory under contract DE-AC52-07NA27344 (LLNL-JRNL-426712).

References

- Anderson, D. L. (1989), *Theory of the Earth*, Blackwell Sci., Malden, Mass.
- Anderson, D. L. (2002), The case for irreversible chemical stratification of the mantle, *Int. Geol. Rev.*, **44**, 97–116.
- Antolik, M., Y. J. Gu, G. Ekström, and A. M. Dziewonski (2003), J362D28: A new joint model of compressional and shear velocity in the Earth’s mantle, *Geophys. J. Int.*, **153**, 443–466.
- Argus, D. F., and R. G. Gordon (1991), No-net-rotation model of current plate velocities incorporating plate motion model NUVEL-1, *Geophys. Res. Lett.*, **18**(11), 2038–2042, doi:10.1029/91GL01532.
- Badro, J., G. Fiquet, F. Guyot, J.-P. Rueff, V. V. Struzhkin, G. Vankó, and G. Monaco (2003), Iron partitioning in Earth’s mantle: Toward a deep lower mantle discontinuity, *Science*, **300**, 789–791.
- Badro, J., J.-P. Rueff, G. Vankó, G. Monaco, G. Fiquet, and F. Guyot (2004), Electronic transitions in perovskite: Possible nonconvecting layers in the lower mantle, *Science*, **305**, 383–386.
- Bassin, C., G. Laske, and G. Masters (2000), The current limits of resolution for surface wave tomography in North America, *EOS Trans. AGU*, **81**, F897.
- Boschi, L., T. W. Becker, G. Soldati, and A. M. Dziewonski (2006), On the relevance of Born theory in global seismic tomography, *Geophys. Res. Lett.*, **33**, L06302, doi:10.1029/2005GL025063.
- Boschi, L., T. W. Becker, and B. Steinberger (2007), Mantle plumes: Dynamic models and seismic images, *Geochem. Geophys. Geosyst.*, **8**, Q10006, doi:10.1029/2007GC001733.
- Brodholt, J. P., G. Helffrich, and J. Trampert (2007), Chemical versus thermal heterogeneity in the lower mantle: The most likely role of anelasticity, *Earth Planet. Sci. Lett.*, **262**, 429–437.
- Cammarano, F., S. Goes, P. Vacher, and D. Giardini (2003), Inferring upper mantle temperatures from seismic velocities, *Phys. Earth Planet. Inter.*, **138**(3–4), 197–222.
- Crowhurst, J. C., J. M. Brown, A. F. Goncharov, and S. D. Jacobsen (2009), Elasticity of (Mg,Fe)O through the spin transition of iron in the lower mantle, *Science*, **319**, 451–453.
- DeMets, C. R., R. G. Gordon, D. F. Argus, and S. Stein (1990), Current plate motions, *Geophys. J. Int.*, **101**(2), 425–478.
- DeMets, C. R., R. G. Gordon, D. F. Argus, and S. Stein (1994), Effect of recent revisions to the geomagnetic reversal time scale on estimates of current plate motion, *Geophys. Res. Lett.*, **21**(20), 2191–2194, doi:10.1029/94GL02118.
- Dziewonski, A. M., and F. Gilbert (1976), The effect of small, aspherical perturbations on travel times and a reexamination of the corrections for ellipticity, *Geophys. J. R. Astron. Soc.*, **44**, 7–17.
- Dziewonski, A. M., and D. L. Anderson (1981), Preliminary reference Earth model, *Phys. Earth Planet. Inter.*, **25**, 297–356.
- Engdahl, E., R. D. van der Hilst, and R. Buland (1998), Global teleseismic earthquake relocation with improved travel times and procedures for depth discrimination, *Bull. Seismol. Soc. Am.*, **88**, 722–743.
- Forte, A. M., and W. R. Peltier (1987), Plate tectonics and aspherical Earth structure: the importance of poloidal-toroidal coupling, *J. Geophys. Res.*, **92**(B5), 3645–3679, doi:10.1029/JB092iB05p03645.
- Forte, A. M., and W. R. Peltier (1994), The kinematics and dynamics of poloidal toroidal coupling in mantle flow: The importance of surface plates and lateral viscosity variations, *Adv. Geophys.*, **36**, 1–119.

- Forte, A. M., W. R. Peltier, A. M. Dziewonski, and R. L. Woodward (1993), Dynamic surface topography: A new interpretation based upon mantle flow models derived from seismic tomography, *Geophys. Res. Lett.*, 20(3), 225–228, doi:10.1029/93GL00249.
- Forte, A. M. (2007), Constraints on seismic models from other disciplines—implications for mantle dynamics and composition, in *Treatise of Geophysics*, vol. 1, pp. 805–858, edited by B. Romanowicz and A. M. Dziewonski, Elsevier, Amsterdam.
- Forte, A. M., and J. X. Mitrovica (2001), Deep mantle high-viscosity flow and thermochemical structure inferred from seismic and geodynamic data, *Nature*, 410(6832), 1049–1056.
- Forte, A. M., and H. K. C. Perry (2000), Geodynamic evidence for a chemically depleted continental tectosphere, *Science*, 290, 1940–1944.
- Forte, A. M., J. X. Mitrovica, and R. L. Woodward (1995), Seismic–geodynamic determination of the origin of excess ellipticity of the core–mantle boundary, *Geophys. Res. Lett.*, 22(9), 1013–1016, doi:10.1029/95GL10165.
- Forte, A. M., S. Quéré, R. Moucha, N. A. Simmons, S. P. Grand, J. X. Mitrovica, and D. B. Rowley (2010), Joint seismic–geodynamic–mineral physical modeling of African geodynamics: A reconciliation of deep mantle convection with surface geophysical constraints, *Earth Planet. Sci. Lett.*, 295, 329–341.
- Grand, S. P. (1994), Mantle shear structure beneath the Americas and surrounding oceans, *J. Geophys. Res.*, 99(B6), 11,591–11,621, doi:10.1029/94JB00042.
- Grand, S. P. (2002), Mantle shear wave tomography and the fate of subducted slabs, *Philos. Trans. R. Soc. London, Ser. A*, 360(1800), 2475–2491.
- Grand, S. P., and D. V. Helmberger (1984), Upper mantle shear structure of North America, *Geophys. J. R. Astron. Soc.*, 76, 399–438.
- Grand, S. P., R. D. Van der Hilst, and S. Widjiantoro (1997), Global seismic tomography: A snapshot of convection in the Earth, *GSA Today*, 7, 1–7.
- Hernlund, J. W., C. Thomas, and P. J. Tackley (2005), A doubling of the postperovskite phase boundary and structure of the Earth's lowermost mantle, *Nature*, 434, 882–886.
- Hernlund, J. W., and C. Houser (2008), On the statistical distribution of seismic velocities in Earth's deep mantle, *Earth Planet. Sci. Lett.*, 265, 423–437.
- Herring, T. A., P. M. Mathews, and B. A. Buffett (2002), Modeling of nutation–precession; very long baseline interferometry results, *J. Geophys. Res.*, 107(B4), 2069, doi:10.1029/2001JB000165.
- Hirose, K. (2006), Postperovskite phase transition and its geophysical implications, *Rev. Geophys.*, 44, RG3001, doi:10.1029/2005RG000186.
- Hofmeister, A. M. (2006), Is low-spin Fe^{2+} present in Earth's mantle?, *Earth Planet. Sci. Lett.*, 243, 44–52.
- Hutko, A. R., T. Lay, J. Revenaugh, and E. J. Garnero (2008), Anticorrelated seismic velocity anomalies from postperovskite in the lowermost mantle, *Science*, 320, 1070–1074.
- Itaka, T., K. Hirose, K. Kawamura, and M. Murakami (2004), The elasticity of the MgSiO_3 postperovskite phase in the Earth's lowermost mantle, *Nature*, 430, 442–445.
- Ingber, L. (1989), Very fast simulated reannealing, *Math. Comput. Model.*, 12, 967–973.
- Ishii, M., and J. Tromp (1999), Normal-mode and free air gravity constraints on lateral variations in velocity and density of Earth's mantle, *Science*, 285(5431), 1231–1236.
- Ishii, M., and J. Tromp (2004), Constraining large-scale mantle heterogeneity using mantle and inner-core sensitive normal modes, *Phys. Earth Planet. Inter.*, 146(1–2), 113–124.
- Jackson, C., M. K. Sen, and P. L. Stoffa (2004), An efficient stochastic Bayesian approach to optimal parameter and uncertainty estimation for climate model predictions, *J. Clim.*, 17, 2828–2841.
- Jordan, T. H. (1978), Composition and development of the continental tectosphere, *Nature*, 274, 544–548.
- Karato, S. I. (1993), Importance of anelasticity in the interpretation of seismic tomography, *Geophys. Res. Lett.*, 20(15), 1623–1626, doi:10.1029/93GL01767.
- Karato, S. I., and B. B. Karki (2001), Origin of lateral variation of seismic wave velocities and density in the deep mantle, *J. Geophys. Res.*, 106(B10), 21,771–21,783, doi:10.1029/2001JB000214.
- Kennett, B. L. N., and A. Gorbatov (2004), Seismic heterogeneity in the mantle—Strong shear wave signature of slabs from joint tomography, *Phys. Earth Planet. Inter.*, 146, 87–100.
- Kennett, B. L. N., S. Widjiantoro, and R. D. van der Hilst (1998), Joint seismic tomography for bulk sound and shear wave speed in the Earth's mantle, *J. Geophys. Res.*, 103(B6), 12,469–12,493, doi:10.1029/98JB00150.
- Khan, A., L. Boschi, and J. A. D. Connolly (2009), On mantle chemical and thermal heterogeneities and anisotropy as mapped by inversion of global surface wave data, *J. Geophys. Res.*, 114, B09305, doi:10.1029/2009JB006399.
- Kuo, C., and B. Romanowicz (2002), On the resolution of density anomalies in the Earth's mantle using spectral fitting of normal-mode data, *Geophys. J. Int.*, 150, 162–179.
- Lay, T., J. Hernlund, E. J. Garnero, and M. S. Thorne (2006), A postperovskite lens and D'' heat flux beneath the central Pacific, *Science*, 314, 1272–1276.
- Lemoine, F. G., et al. (1998), The development of the joint NASA GSFC and NIMA Geopotential Model EGMM96, *NASA Tech. Rep.*, 1998–206861.
- Le Stunff, Y., and Y. Ricard (1995), Topography and geoid due to lithospheric mass anomalies, *Geophys. J. Int.*, 122, 982–990.
- Lin, J.-F., G. Vankó, S. D. Jacobsen, V. Iota, V. V. Struzhkin, V. V. Prakapenka, A. Kuznetsov, and C.-S. Yoo (2007), Spin transition zone in Earth's lower mantle, *Science*, 317, 1740–1743.
- Lin, J.-F., H. Watson, G. Vankó, E. E. Alp, V. V. Prakapenka, P. Dera, V. V. Struzhkin, A. Kubo, J. Zhao, C. McCammon, and W. J. Evans (2008), Intermediate-spin ferrous iron in lowermost mantle postperovskite and perovskite, *Nat. Geosci.*, 1, 688–691.
- Masters, G., G. Laske, H. Bolton, and A.M. Dziewonski (2000), The relative behavior of shear velocity, bulk sound speed, and compressional velocity in the mantle: Implications for chemical and thermal structure, in *Earth's Deep Interior: Mineral Physics and Tomography from the Atomic to the Global Scale*, edited by S.-I. Karato et al., pp. 63–87, AGU, Washington, D. C.
- Matas, J., and M. Bukowinski (2007), On the anelastic contribution to the temperature dependence of lower mantle seismic velocities, *Earth Planet. Sci. Lett.*, 259, 51–65.
- Mathews, P. M., T. A. Herring, and B. A. Buffett (2002), Modeling of nutation and precession: New nutation series for nonrigid Earth and insights into the Earth's interior, *J. Geophys. Res.*, 107(B4), 2068, doi:10.1029/2001JB000390.
- McCammon, C., I. Kantor, O. Narygina, J. Rouquette, U. Ponkratz, I. Sergueev, M. Mezouar, V. Prakapenka, and L. Dubrovinsky (2008), Stable intermediate-spin ferrous iron in lower mantle perovskite, *Nat. Geosci.*, 1, 684–687.
- McNamara, A. K., and S. Zhong (2005), Thermochemical structures beneath Africa and the Pacific Ocean, *Nature*, 437(7062), 1136–1139.
- Mitrovica, J.X. and A.M. Forte (2004), A new inference of mantle viscosity based upon joint inversion of convection and glacial isostatic adjustment data, *Earth Planet. Sci. Lett.*, 225(1–2), 177–189.
- Montelli, R., G. Nolet, F. A. Dahlen, G. Masters, E. R. Engdahl, and S.-H. Hung (2004), Finite frequency tomography reveals a variety of plumes in the mantle, *Science*, 303, 338–343.
- Mooney, W. D., G. Laske, and G. Masters (1998), CRUST 5.1: A global crustal model at 5 × 5 degrees, *J. Geophys. Res.*, 103(B1), 727–747, doi:10.1029/97JB02122.
- Moucha, R., A. M. Forte, J. X. Mitrovica, and A. Daradich (2007), Lateral variations in mantle rheology: Implications for convection related observables and inferred viscosity models, *Geophys. J. Int.*, 169, 113–135.
- Murakami, M., K. Hirose, K. Kawamura, N. Sata, and Y. Ohishi (2004), Post-perovskite phase transition in MgSiO_3 , *Science*, 304, 855–858.
- Ni, S. D., and D. V. Helmberger (2003), Seismological constraints on the South African superplume; could be the oldest distinct structure on Earth, *Earth Planet. Sci. Lett.*, 206(1–2), 119–131.
- Ni, S. D., E. Tan, M. Gurnis, and D. V. Helmberger (2002), Sharp sides to the African superplume, *Science*, 296(5574), 1850–1852.
- Oganov, A. R., and S. Ono (2004), Theoretical and experimental evidence for a postperovskite phase of MgSiO_3 in Earth's D'' layer, *Nature*, 430, 445–448.
- Paige, C. C., and M. A. Saunders (1982), LSQR: An algorithm for sparse linear equations and sparse least squares, *ACM Trans. Math. Software*, 8, 43–71.
- Peter, D., L. Boschi, and J. H. Woodhouse (2009), Tomographic resolution of ray and finite frequency methods: A membrane-wave investigation, *Geophys. J. Int.*, 177, 624–638.
- Quéré, S., and A. M. Forte (2006), Influence of past and present-day plate motions on spherical models of mantle convection: Implications for mantle plumes and hot spots, *Geophys. J. Int.*, 165, 1041–1057.
- Ricard, Y., L. Fleitout, and C. Froidevaux (1984), Geoid heights and lithospheric stresses for a dynamic Earth, *Ann. Geophys.*, 2, 267–286.
- Richards, M. A., and B. H. Hager (1984), Geoid anomalies in a dynamic Earth, *J. Geophys. Res.*, 89(B7), 5987–6002, doi:10.1029/JB089iB07p05987.
- Ritsema, J., and H. H. van Heijst (2002), Constraints on the correlation of P and S wave velocity heterogeneity in the mantle from P , PP , PPP and $PKPab$ traveltimes, *Geophys. J. Int.*, 149, 482–489.
- Ritsema, J., H. J. Van Heijst, and J. H. Woodhouse (1999), Complex shear wave velocity structure imaged beneath Africa and Iceland, *Science*, 286(5446), 1925–1928.

- Robertson, G. S., and J. H. Woodhouse (1996), Ratio of relative S to P velocity heterogeneity in the lower mantle, *J. Geophys. Res.*, 101(B9), 20,041–20,052, doi:10.1029/96JB01905.
- Saltzer, R. L., R. D. Van der Hilst, and H. Kárasoñ (2001), Comparing P and S wave heterogeneity in the mantle, *Geophys. Res. Lett.*, 28(7) 1335–1338, doi:10.1029/2000GL012339.
- Schubert, B. S. A., H. P. Bunge, and J. Ritsema (2009), Tomographic filtering of high-resolution mantle circulation models: Can seismic heterogeneity be explained by temperature alone?, *Geochem. Geophys. Geosyst.*, 10, Q05W03, doi:10.1029/2009GC002401.
- Simmons, N. A., A. M. Forte, and S. P. Grand (2006), Constraining mantle flow with seismic and geodynamic data: A joint approach, *Earth Planet. Sci. Lett.*, 246, 109–124.
- Simmons, N. A., A. M. Forte, and S. P. Grand (2007), Thermochemical structure and dynamics of the African superplume, *Geophys. Res. Lett.*, 34(2), L02301, doi: 10.1029/2006GL028009.
- Simmons, N. A., A. M. Forte, and S. P. Grand (2009), Joint seismic, geo-dynamic and mineral physical constraints on three-dimensional mantle heterogeneity: Implications for the relative importance of thermal versus compositional heterogeneity, *Geophys. J. Int.*, 177(5), 1284–1304.
- Soldati, G., L. Boschi, F. Deschamps, and D. Giardini (2009), Inferring radial models of mantle viscosity from gravity (GRACE) data and an evolutionary algorithm, *Phys. Earth Planet. Inter.*, 176, 19–32.
- Speziale, S., V. E. Lee, S. M. Clark, J.-F. Lin, M. P. Pasternak, and R. Jeanloz (2007), Effects of Fe spin transition on the elasticity of (Mg, Fe)O magnesiowüstites and implications for the seismological properties of the Earth's lower mantle, *J. Geophys. Res.*, 112, B10212, doi:10.1029/2006JB004730.
- Stackhouse, S., J. P. Brodholt, and G. D. Price (2007), Electronic spin transitions in iron-bearing MgSiO_3 perovskite, *Earth Planet. Sci. Lett.*, 253, 282–290.
- Su, W., and A. M. Dziewonski (1993), Joint 3-D inversion for P and S velocity in the mantle, *EOS Trans. AGU*, 74, 557.
- Su, W., and A. M. Dziewonski (1997), Simultaneous inversion for 3-D variations in shear and bulk velocity in the mantle, *Phys. Earth Planet. Inter.*, 100(1–4), 135–156.
- Trampert, J., F. Deschamps, J. Resovsky, and D. Yuen (2004), Probabilistic tomography maps chemical heterogeneities throughout the lower mantle, *Science*, 306(5697), 853–856.
- Tsuchiya, T., J. Tsuchiya, K. Umemoto, and R. M. Wentzcovitch (2004), Elasticity of postperovskite MgSiO_3 , *Geophys. Res. Lett.*, 31, L14603, doi:10.1029/2004GL020278.
- Van der Hilst, R. D., and H. Kárasoñ (1999), Compositional heterogeneity in the bottom 1000 kilometers of the Earth's mantle: Toward a hybrid convection model, *Science*, 283, 1885–1888.
- Vasco, D. W., L. R. Johnson, R. J. Pulliam, and P. S. Earle (1994), Robust inversion of IASP91 traveltimes residuals for mantle P and S velocity structure, earthquake mislocations, and station corrections, *J. Geophys. Res.*, 99(B7), 13,727–13,755, doi:10.1029/93JB02023.
- Wen, L. X. (2001), Seismic evidence for a rapidly varying compositional anomaly at the base of the Earth's mantle beneath the Indian Ocean, *Earth Planet. Sci. Lett.*, 194(1–2), 83–95.
- Wen, L. X., and D. L. Anderson (1997), Present-day plate motion constraint on mantle rheology and convection, *J. Geophys. Res.*, 102(B11), 24,639–24,653, doi:10.1029/97JB02159.
- Wentzcovitch, R. M., J. F. Justo, Z. Wu, C. R. S. da Silva, D. A. Yuen, and D. Kohlstedt (2009), Anomalous compressibility of ferropericlase throughout the iron spin cross-over, *Proc. Natl. Acad. Sci.*, 106(21), 8447–8452.
- Wookey, J., S. Stackhouse, J.-M. Kendall, J. Brodholt, and G. D. Price (2005), Efficacy of the postperovskite phase as an explanation of lower-most mantle seismic properties, *Nature*, 438, 1004–1008.
- L. Boschi, Eidgenössische Technische Hochschule Hönggerberg, Institute of Geophysics, Schafmattstr. 30, 8093 Zurich, Switzerland.
- A. M. Forte, GEOTOP, Département des Sciences de la Terre et de l'Atmosphère, Université du Québec à Montréal, CP 8888, Succursale Centre-Ville, Montréal, QC H3C 3P8, Canada.
- S. P. Grand, Jackson School of Geosciences, University of Texas at Austin, Austin, TX 78712, USA.
- N. A. Simmons, Atmospheric, Earth and Energy Division, Lawrence Livermore National Laboratory, 7000 East Ave., L-046, Livermore, CA 94550, USA. (Simmons27@llnl.gov)